# Master thesis

## Development of a slitless spectrometer for multispectral flame chemiluminescence

Shuaidong Yu

Technische Universiteit Delft

**T**U**Delft**

Delft
University of
Technology

**Challenge the future**

# MASTER THESIS

## DEVELOPMENT OF A SLITLESS SPECTROMETER FOR MULTISPECTRAL FLAME CHEMILUMINESCENCE

by

## Shuaidong Yu

in partial fulfillment of the requirements for the degree of

**Master of Science**

in Aerospace Engineering

at the Delft University of Technology,
to be defended publicly on Thursday June 21, 2018 at 9:00 AM.

| | | |
|---|---|---|
| Supervisor: | Dr. ir. Alexis Bohlin | |
| Thesis committee: | Dr. Arvind. Gangoli. Rao (Chairman), | TU Delft |
| | Dr. ir. Ferdinand. Schrijer, | TU Delft |

An electronic version of this thesis is available at http://repository.tudelft.nl/.

# PREFACE

This thesis report has been made as a completion of my master education at the faculty of aerospace engineering of Delft University of Technology. With the submission of this thesis report, almost three years of study and research as a master student comes to a great end. My master education at TUDelft has really helped be become a creative, passionate, and independent researcher.

I would firstly like to take this opportunity to thank my supervisor Dr. ir. Alexis Bohlin for his patient and inspiring supervision. Thanks to his open mind, I have discovered my special characteristics and skills in not only a scientific research but also daily life.

Furthermore, I would like to thank all the lab technicians: Dennis, Peter and Henk-Jan for their kind help in the lab and the mechanical workshop.

Finally, I would also express my special thanks to my families and friends. Thanks for their love and consistent support over the years.

<div align="right">

*Shuaidong Yu*
*Delft, June 2018*

</div>

# ABSTRACT

Currently, combustion of fossil fuels still accounts for the majority of the worldwide energy support. The resulting air pollution has thus drawn an increasing public attention. Some short-lived intermediate radical species OH, CH, $C_2$, and CN have long been proved to be essential in forming combustion pollutants. To study these radicals, served as one of the most commonly-used techniques, flame emission spectroscopy is still strongly dependent on the conventional slit spectrometer, which provides an extremely limited view of the flame. Although a scanning method can be used to reconstruct the image in order to compensate for this disadvantage, it is limited to only measuring a stable flame that has a relatively time-invariant shape. Therefore, to obtain the flame chemiluminescence information simultaneously from the entire flame, some attempts of snapshot spectrometer arise. However, in the current snapshot design, the image skewing caused by the snapshot imaging system remains unrevealed. The spatial distribution of the chemiluminescence information could ,therefore, be seriously distorted and untrustworthy.

In this thesis, the author has thoroughly proved the feasibility of a snapshot or in another word slitless spectrometer. Two experimental setups are proposed in this thesis. The first setup, monochromatic synthetic flame design, is used to study the image skewing effect of a slitless spectrometer while the second setup, after the image skewing effect has been well-understood, is proposed to study the spatial distribution of the intermediate radicals CH and $C_2$.

During the investigation process, the image skewing effect in the imaging process of a slitless spectrometer has been explored both theoretically and experimentally, which shows an excellent agreement. It has been found that the image skewing mainly results from the diffraction grating, and this effect is called an ananmorphic magnification, which can be totally eliminated by using Littrow configuration of the diffraction grating. By analyzing the spatial distribution of CH ($431nm$) and $C_2$ ($514nm$) captured by the slitless spectrometer, it has been found that their spatial distributions are slightly different. When the equivalence ratio is equal to 1.2, the spectral image of $C_2$ ($514nm$) has a shorter height while a longer bottom.

*Keywords:*
*combustion, chemiluminescence, spectrometer, scanning, snapshot, slitless, imaging, lens aberration,*
*anamorphic magnification*

# CONTENTS

# LIST OF FIGURES

# 1

# INTRODUCTION

## 1.1. RESEARCH BACKGROUND AND MOTIVATION

Since air pollution caused by the burning of fossil fuels is of great environmental concern, reducing combustion emissions and increasing combustion efficiency have been drawing many researchers attention. Generally, flue gas is used to analyze combustion emissions, however there is always a delay between the combustion process at a specific time point and the obtainment of the flue gas generated from the same time point[20]. As a result, the analysis of immediate burner conditions, an essential part of combustion diagnostics, cannot be revealed by flue gas analysis. Therefore, in order to tackle this problem, an alternative strategy to determine combustion emissions appears, which correlates the combustion emissions with certain short-lived intermediate radical species in flames. According to Gaydon, several intermediate radical species, for example, OH, CH, $C_2$ and CN have been established to be vital in forming combustion pollutants such as $NO_X$ and unburnt particles[21].

Currently, there are multiple techniques used to detect these intermediate species with the most common ones being flame emission spectroscopy and laser-based diagnosing techniques[20, 22–25]. The major difference between the two techniques is that flame emission spectroscopy is a non-intrusive passive technique similar to a spectrum signal receiver, while the laser based techniques, in addition to the "spectrum signal receiver", also require an external laser source to excite these species, which may be intrusive to the flame structure too. Presently, because of the ability to obtain real quantitative results for laser-based techniques, they have nearly totally replaced the flame emission spectroscopy techniques in combustion monitoring[26]. However since laser-based techniques always request more complex setups, the simple and easily-used flame emission techniques turn out to be more desirable in some industrial environments and they have been rejuvenated recently in many papers for active combustion control[26].

For emission spectroscopy techniques, normally a spectrometer with a slit is implemented[27–30]. Three well-known textbooks on spectrometer design and flame emission spectroscopy are also based on the slit[21, 31, 32], although the concept of slitless spectrometer is also briefly mentioned in the first textbook[31]. One main disadvantage of this slit spectrometer is the extremely limited field of view. As we know, a spectrometer always requires an image of the object formed on the entrance slit. Therefore consequently, only a slit of the image can be captured and analyzed at once. In spite of the fact that the limited field of view can be solved by scanning along the object and then reconstructing the image as shown in this paper[27], the reconstructed image is however not taken in the same time point. To make things worse, if the target is an unstable flame, such as a turbulence flame, whose shape changes frequently along with time, the reconstructing process will become extremely hard. The scanning method is feasible only if the scanning time is small enough to actually freeze the shape of a flame. Therefore, in order to solve this problem, a slitless or in another word snapshot spectrometer design is proposed in this project, which gives a whole field of view of the flame and allows simultaneous capturing of all spectral images of relevant radicals.

## 1.2. RESEARCH OBJECTIVE AND QUESTIONS

The main research objective is to design a slitless spectrometer that can be used to study the chemiluminescence of various radicals for a Bunsen flame simultaneously by analyzing the whole field of view of the conical flame. For achieving this main objective, several sub-goals need to be specified:

1. To understand what flame emission spectroscopy is and how the spectrum of a Bunsen flame is formed by certain intermediate radicals.

2. To validate the concept of slitless spectrometer and understand the difference between it and a conventional slit spectrometer.

3. To investigate the imaging process of a slitless spectrometer and understand all possible aberrations in the process and how to reduce them.

Based on the design objective, three main research questions followed by several sub-questions can be derived:

1. What is flame emission spectroscopy?

    • What is a flame?
    • What is flame chemiluminescence?
    • How is a flame emission spectrum formed?

2. How to design a slitless spectrometer?

    • What is a conventional spectrometer usually made up of?
    • What is the working principle of each component in a normal spectrometer?
    • What is the difference between a normal slit spectrometer and a slitless spectrometer?

3. How to calibrate a slitless spectrometer?

    • What are the possible aberrations caused by an imaging system?
    • How a spectral image is actually skewed by a slitless spectrometer?
    • How to reduce and correct the skewing of spectral images?

## 1.3. REPORT OUTLINE

This report is composed of 6 chapters, the main part of which starts from chapter 2. Chapter 2 to 4 will give readers some literature review and relevant background knowledge for this research. The first research question will be answered thoroughly in chapter 2 and 3. Chapter 4 will mainly discuss the second research question and the key concept of collimation used for a slitless spectrometer will also be defined in this chapter. During the discussion of imaging process in chapter 4, lens aberration and grating anamorphic magnification will also be studied in details, which provides a strong background for understanding the skewing of spectral images in the slitless spectrometer. After obtaining a deep understanding of all the physics and concepts, chapter 5 and 6 will be the main content of this research, presenting the experimental setup and results. Finally, the last chapter will draw a conclusion of this research and provides some directions for future research.

<div style="text-align: right; font-size: 3em; font-weight: bold;">2</div>

# FLAME EMISSION SPECTROSCOPY

## 2.1. COMBUSTION AND FLAME

Combustion, one of the oldest technologies of human beings, has been using for more than 1 million years and it contributes to 90% of the worldwide energy support in present days. Combustion is a type of chemical reaction that is essentially the rearrangement and exchange of atoms through molecule collisions and flame is the emission of light through this process[21]. When a combustion reaction happens, fuels and oxidizers react with each other, producing products that are often gaseous and simultaneously releasing heat, which turns out to be the main interest of combustion.

In combustion process, fuels and oxidizers are mixed and burnt. Depending on whether the fuels and oxidizers are mixed before burning, the flame can be divided into two categories: premixed flame and non-premixed (diffusion) flame. A flame is called premixed flame if fuels and oxidizers (typically air) are mixed before burning. A Bunsen flame and a flat flame are two examples of this category. However, if the fuels and oxidizers are mixed and burnt at the same time, it is called non-premixed (diffusion) flame (fuel and oxidizers are mixed by diffusion). In this category, a candle flame and the flame in an aeroengine combustion chamber are two typical examples. Furthermore, depending on whether the gaseous flow of the fuels and air is laminar or turbulent, the flame can also be subdivided into laminar flame and turbulent flame. With increased flow velocity, transition from laminar to turbulent may take place, as demonstrated in the figure below, taking a diffusion flame for instance.
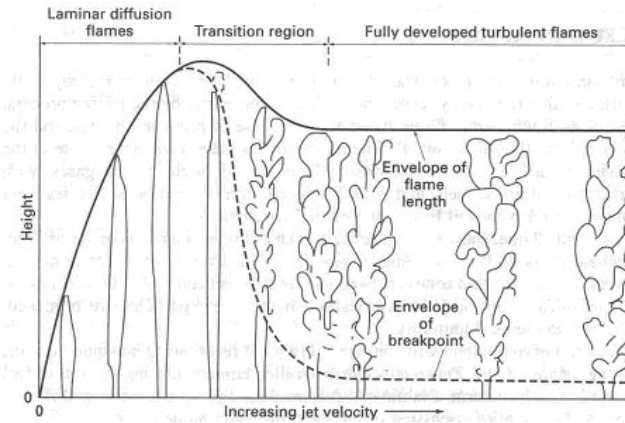


Figure 2.1: A demonstration of flow transition from laminar to turbulent in a diffusion flame[1].

A premixed flame is stoichiometric when fuels and oxidizers consume each other completely. The equivalence ratio $\phi$ is the ratio between the real fuel-oxidizer ratio and the stoichiometric fuel-oxidizer ratio, as given in the equation below:

$$\phi = \frac{(m_{fuel}/m_{oxidizer})_{real}}{(m_{fuel}/m_{oxidizer})_{st}}$$

<div style="text-align: center;">3</div>

A fuel-rich flame is the flame with extra fuels, which means that $\phi > 1$. Fuel-lean flame is the flame when there is an excess of oxidizers, which means that $\phi < 1$.

The most noticeable feature of Bunsen flame is the bright flame cone, which is the reaction zone where the most intensive chemical reactions happen, as shown in the figure below. The unburnt fuel and air are inside this conical shape and for a fuel-rich burning condition, as is shown in the figure below, there is also excessive fuel that is mixed with ambient air, leading to a second diffusion flame outside this cone.
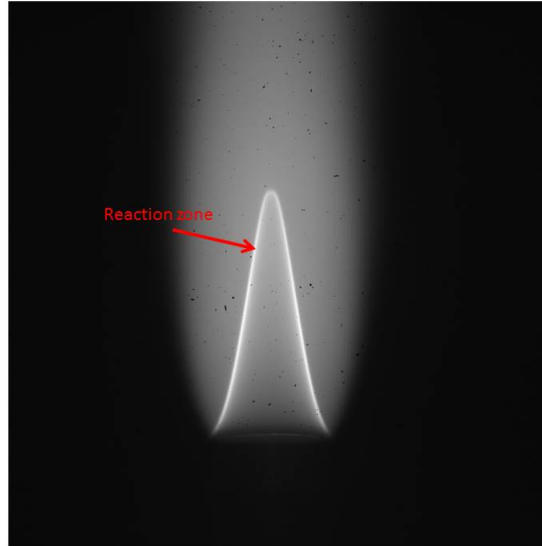


Figure 2.2: A fuel-rich Bunsen flame whose equivalence ratio is 1.2. The 2D reaction zone is represented as the brightest conical curve.

Taking a photo of an object is actually converting the 3D object into a 2D image, so the image on the camera sensor is actually a projection of an object, as demonstrated in the figure below. The image of the Bunsen flame is essentially an integration of a portion of the reaction zone. This also explains why the conical flame has a relatively brighter edge in comparison to the central area.
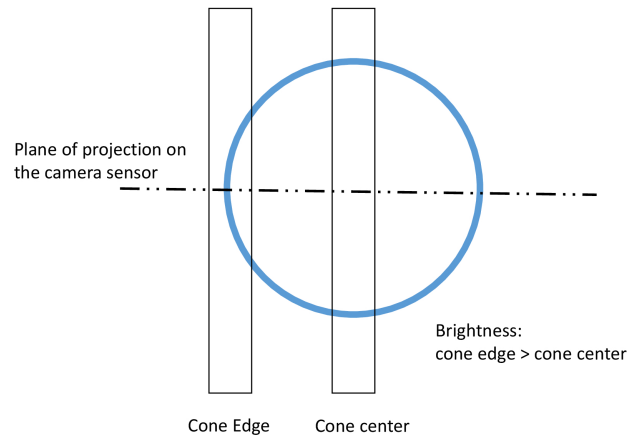


Figure 2.3: A schematic diagram of the reaction zone projection, top view of the Bunsen flame. Compared with the cone center, a larger portion of reaction zone is integrated in the cone edge.

## 2.2. EMISSION SPECTRA OF FLAMES

The flame emits energy in the form of electromagnetic radiation caused by molecular energy transitions as will be discussed in next chapter. The collection of different transitions leads to various radiated wavelengths, thus forming an emission spectrum. The radiation can fall into either the visible domain or the infrared and ultraviolet domains. The emission in ultraviolet and visible domain of the flame spectrum, the major interest of this research, is caused by minor side reactions between free radicals. For clean flames the radiation in the visible and ultraviolet domain usually accounts for less than 0.4 % of the overall heat generated in combustion, which means the most of the heat release comes from the IR domain of the spectrum[26].

The ordinary molecules such as $CO_2$, $H_2O$, CO, $O_2$ or $N_2$ are always the stable products of combustion. They do not give spectra that have considerable strength in the visible or ultraviolet domains[26]. This is because the main resonance transitions of these molecules lay far down in the UV region so that usually the energy in flames is not sufficient to excite these spectra[21]. However, the intermediate products of combustion—free radicals such as CH, OH, $C_2$, CN, and NH, as a result of relatively low excitation energy, do possess appreciable strength in the visible or near ultraviolet regions[21]. These free radicals are responsible for the most prominent characteristics in flames.

The emission spectra radiated by the flame can be categorized into two types basically, i.e. , continuous spectra and discontinuous spectra.

For a flame, the continuous spectra are in most cases perceived in the luminous region where radiative energy released by soot and other solid particles complies with the Planck radiation theory and this type of spectra are always distributed over a broad spectral range in a common mode [20]. Among this group, the spectrum emitted by the sun is a typical example.

The discontinuous spectra are assigned to isolated atoms or intermediate radical species in the flame. A quantity of intermediate radical species are generated in their excited electronic states when the fuel reacts with oxygen at high temperature, and they are featured by strong spectral bands [20].

The discontinuous spectra can also be further classified into two categories: line spectrum (atomic spectrum), which is attributed to free atoms, and band spectrum, which is attributed to the species that has chemical bonds, as will be depicted in next chapter, such as free molecules and free radicals. For each line in line spectra, it corresponds to one electronic transition from one energy level to another energy level. However the band spectra are caused by not only electronic transition but also the other two rotational and vibrational transitions and the detailed reason will be discussed in next chapter. Within one band, the spectra of diatomic molecules always have one sharp edge (band head) with the maximum intensity and gradually fades to the other end. Since each species in the flame has a unique spectrum, their spectra can be used to identify themselves in the flame.

## 2.3. EMISSION SPECTRA OF SOME SPECIES

Before getting into the details of the spectra, it is worth understanding how the light of a particular wavelength is generated. These spectra are formed through a process called chemiluminescense, which is the emission of cold light (luminescence) as a result of chemical reactions (chemi-). Taking the formation of OH for example, as demonstrated in the two equations below. One excited radical $OH^*$ is firstly formed. Then the unstable excited radical decays from the excited state to the ground state, emitting one photon that has a particular wavelength. The emitted photons or light thus forms the emission spectra.

$$CH + O_2 \rightarrow CO + OH^*$$

$$OH^* \rightarrow OH + h\nu$$
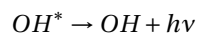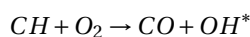
### 2.3.1. OH SPECTRUM

In many types of flame, the hydroxyl radical (OH) is an abundant species. It is formed in the reaction zone, and persists beyond that in quasi-equilibrium with water vapor. Because of its formation history, it provides information on the location of the reaction zone, and it is always used as an accepted flame front marker[33].

Therefore it is of interest to experimentally quantify the hydroxyl radical distribution in a flame. There are three band systems attributed to the OH spectrum, among which the ultraviolet band system is the only one identified in flames, thus drawing great attention of combustion diagnostics. The existence of the OH radical is identified through the ultraviolet band system that has a widely open structure whose the strongest band head lies at $\lambda = 306.4 nm$ [26].

### 2.3.2. CH SPECTRUM

CH is formed near the first sharp temperature rise in the reaction zone, having a blue or violet color. CH basically has three band systems, among which the strongest band system locates around $\lambda = 431.5nm$. It is therefore often referred as the $431.5nm$ system. This $431.5nm$ system is mainly composed of one violet-degrading band that has two band heads at $431.25nm$ and $431.50nm$, which usually can not be discerned. The second strongest band system locates at near UV region, which is around $390nm$ as tested by the author. This second band system always has a very weak signal so that it is hard to be discerned sometimes.

### 2.3.3. $C_2$ SPECTRUM

$C_2$ radical has 7 known band systems. Even though all of the 7 band systems can be perceived in the inner cone of acetylene flames, the most typical features of $C_2$ in all kinds of hydrocarbon flames are produced by Swan bands (from 435.0 to 686.0$nm$), which has the characteristic blue-green color[26]. All the bands within the swan band system are degrading toward the violet and the strongest band head locates at $\lambda = 514nm$.

The spectrum in the visible range collected in a fuel-rich Bunsen flame with the equivalence ratio being 1.2 is shown below for easy reference.
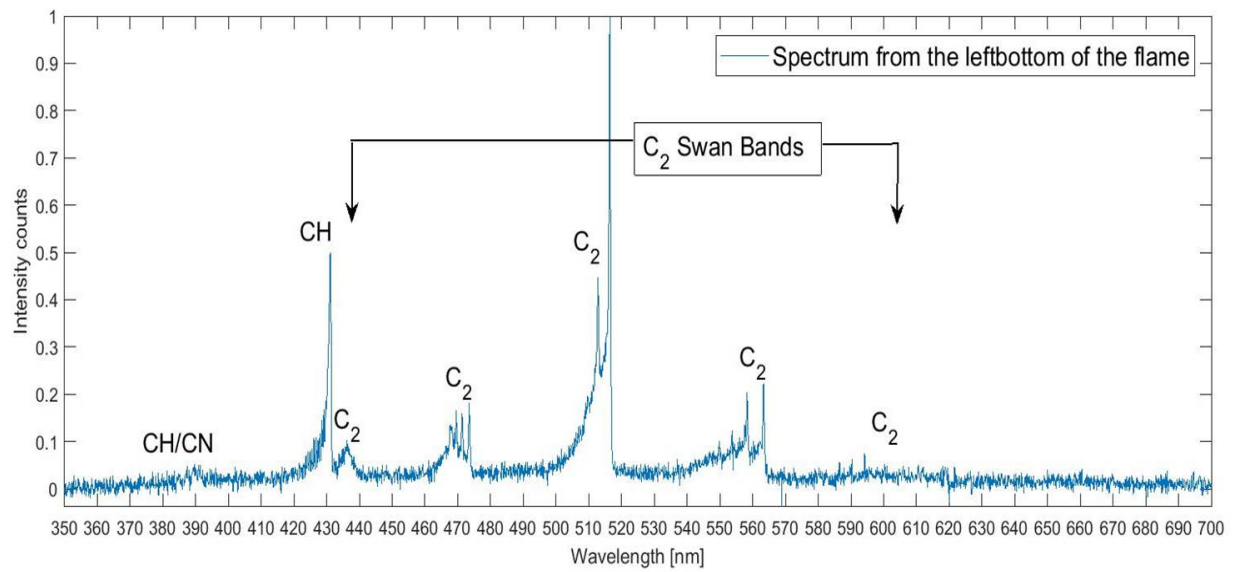


Figure 2.4: A demonstration of the CH band system and $C_2$ swan band system, captured under the equivalence ratio 1.2.

# 3

# MOLECULAR PHYSICS

In order to have a thorough understanding of emission spectra of flames, it is necessary to have a knowledge of the molecular structure and the interaction between photons and molecules. Since the main interest in this research focuses on optical system design and spectroscopy, only the content of molecular structure and internal energy of molecules are covered in this chapter, which should give readers a sufficient background to understand the emission spectra of flames in this thesis.

## 3.1. MOLECULAR STRUCTURE AND BONDING

A molecule is composed of at least 2 atoms that connected with each other through chemical bonds. There are many types of chemical bonds, however the mechanism of forming them is quite similar, which is due to the attraction of atoms. An atom basically consists of a positively charged nucleus and many electrons with the same amount of negative charge that fill out the space around the nucleus. A nucleus is made up of multiple positively-charged protons and electrically-neutral neutrons. The number of protons a nucleus has, $Z$, is defined as its atomic number. A nucleus typically contains $\geq Z$ neutrons, and 1 electrically neutral atom also contains $Z$ electrons[34].

The typical size of the nuclei is on the order of $10^{-14} - 10^{-15} m$, while the atomic size is on the order of $10^{-10} m$ [34]. Therefore, the nuclei can be considered to be a point mass. In an atom, the spatial distribution of electrons is not uniform. According to statistics, electrons are distributed in one or several spherical shells surrounding the nucleus, which are separated by regions of relatively low electron density. Since the inner shell of electrons is the closest to the nucleus, they are strongly bounded to nucleus. On the other hand, since the electrons in the outermost shell are relatively far away from the nucleus, their bonding is relatively weak. As a result, it is the electrons in the outermost shell which are also called valence electrons that determine the chemical reactivity of atoms. In this way, an atom can be treated as two parts: firstly an atomic core, including nucleus and all electrons in inner shells and secondly the valence electrons in the outermost shell.

Atoms are most stable when their outermost shell is filled up with electrons. However, not all atoms have enough electrons filling their outermost shells. For instance, oxygen atoms only have 6 electrons in their outermost shells which can hold 8 electrons when filled up and hydrogen atoms also need one more electron to become stable. In order to achieve a stable electron configuration, atoms form chemical bonds with each other by interaction and redistribution of their valence electrons in a way of donating, accepting, or sharing valence electrons.When two or more atoms have chemical bonds with each other, a molecule is created. This can also be used to explain chemical reactions between molecules. When two molecules meet, their valence electrons are interacted and redistributed in order to obtain stable configurations, which may also cause possible relocation of atomic cores. The figure below demonstrates a chemical reaction between hydrogen molecules and oxygen molecules from the valence electrons point of view.
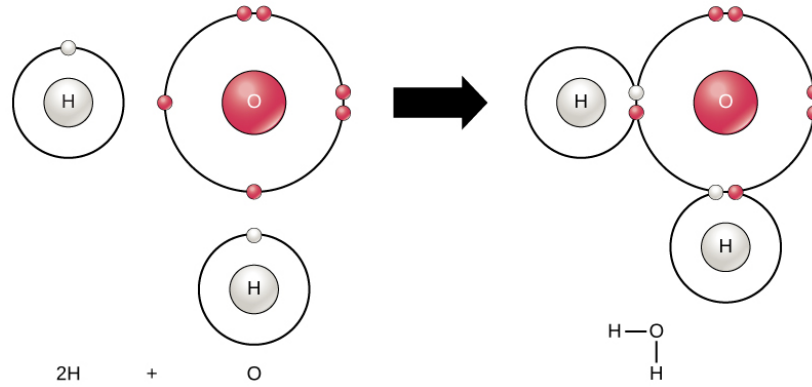
Figure 3.1: How valence electrons are redistributed when 2 hydrogen atoms react with 1 oxygen molecule[1].

## 3.2. Molecular energy levels

The focus of this research is on optical diagnostics of flames which is based on absorption, emission and scattering of photons. The energy is always conserved in the interaction of photons with molecules therefore it is necessary to know the energy of photons and the energy of molecules.The molecules occupy specific energy levels that are discrete. In this way, the energies of photons that can be absorbed or emitted must also be discrete, which means that not every photon can be absorbed or emitted by a molecule.

A molecule has multiple degrees of freedom, including transnational motion of the molecule itself, tumbling motion of molecules, the oscillatory motion of atoms or groups of atoms in a molecule. Among them, only the vibration and rotation contribute to the internal energy of molecules, however, in a relatively small amount. The major part of the internal energy of molecules come from the electronic energy of each atom inside the molecule. The formula below demonstrates their relations.

$$E_{internal} = E_{electronic} + E_{vibration} + E_{rotation}$$

The typical values for each contribution is that electronic energy has around $10^{-19}J$, vibrational energy has around $10^{-20}J$, rotational energy has around $10^{-23}J$[34]. Each molecule is in a specific rotational state, a specific vibrational energy level, and a specific electronic energy level at a certain time. The electronic transitions are always accompanied by a number of vibrational and rotational transitions, and the vibrational transitions are always accompanied by a number of rotational transitions. It is this feature that gives molecules way more possibilities of transitions than the atomics do. In the following paragraphs, each energy will be explained in detail. For making the relation more intuitive, a schematic diagram showing 2 electronic states is given below.
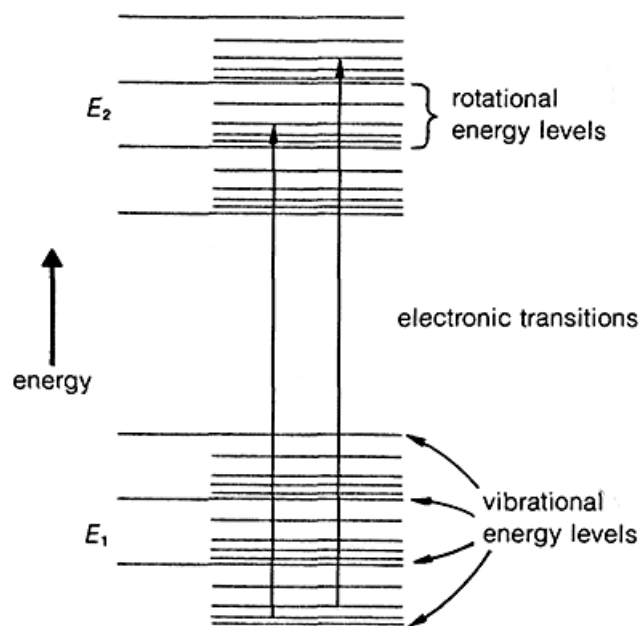
Figure 3.2: A schematic demonstration of electronic, vibrational, and rotational energy levels (The vertical scale is significantly distorted for a better view)[1]. The electronic energy transitions are always accompanied by vibrational and rotational energy level change, which creates more possibilities of transitions (multiple lines within a band) between 2 electronic energy states.

### 3.2.1. ELECTRONIC ENERGY

It is well-known that in atoms, electrons are able to undergo electron transitions under proper conditions. Now in the same way electrons in molecules can also undergo transitions in energy. Though the energy of the valence electrons have been changed after a molecule is formed, these electrons can still undergo energy level transitions as they normally do inside atoms. In this way, if a photon of just a right frequency is provided to the molecule, the electron can jump to an excited state in that molecule and release the same amount of energy when returning back to the ground molecular state.

Just like the unique line spectrum in an atom, an molecule also has an unique spectrum which is called band spectrum or molecular spectrum. Unlike the line spectrum that has distinctly distributed lines, the band spectrum has multiple lines which are continuous and closely spaced to each other by dark spaces. In appearance, each group of lines looks like a "band" so they have the name band spectrum. A band spectrum system sometimes consists of multiple bands. For example, the famous swan band system, one of the 7 known band systems in $C_2$ spectrum, is composed of 5 band groups. These bands can be used to identify which the molecule is just like the line spectrum used in identifying atoms.

The reason that causes the band spectra is, unlike the pure electronic energy transitions in atoms, in molecules the electronic energy transitions are always accompanied by vibrational and rotational energy level change, which creates more possibilities of transitions (multiple lines within a band) between 2 electronic energy states. Because electronic energy levels are generally widely spaced, the emitted light always has large frequencies and therefore situated in the visible or ultra-violet region. The figure below gives reader an intuitive view of the difference between line spectrum (atom) and band spectrum (molecule).

(a) Line spectrum
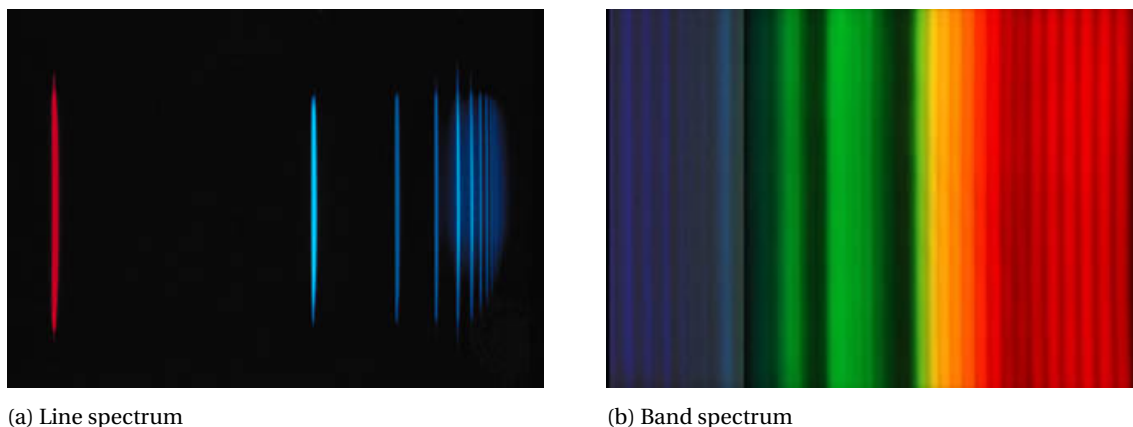


(b) Band spectrum

Figure 3.3: Examples of line spectrum and band spectrum [1].

### 3.2.2. VIBRATIONAL ENERGY

When atoms form a molecule, the atoms inside can also vibrate. For example, a diatomic molecule can be treated as two marbles connected by a spring, as demonstrated in figure 3.4. Vibrational energy levels from 0 to 6 are indicated in the figure. Higher numbers mean higher energy levels and greater vibrational amplitude. If there is a change in vibrational energy that is exactly the difference between two vibrational energy levels (by absorbing or emitting photons), the molecule can transition to a new vibrational level.

When two atoms combine to form a molecule, the energy of the molecule is typically less than the sum of the energies of individual atoms. This is due to the overlap of electron clouds and in this way, the molecule reaches a more stable state, which is also the reason why atoms tend to form molecules.

For simplification, only the diatomic molecule is treated here, which only has a single vibrational mode, namely stretching of the bond between the two atoms. When the internuclear distance is not too far from the equilibrium value $r_e$, the potential energy curve can be approximated as a parabola that is called harmonic oscillator approximation, as shown in the figure 3.4. The energy is thus given by:

$$E_{vibration} = hf(v + \frac{1}{2})$$

Where $h$ is Planck constant, $f$ is the vibrational frequency, and $v$ is the vibrational quantum number which begins with 0 and increases by the increment of 1. Since $v$ is discrete, the vibrational energy is also quantized. As can be observed in the figure, the intermoelcular distance rises with the increase of vibrational quantum number $v$ (for example from 0 to 6), indicating the vibrational energy is increased. vibrational transitions are always accompanied by rotational transitions, thus in vibrational transitions or vibration-rotation transitions, the molecule transits both from one vibrational and one rotational level to a new vibrational and rotational energy level, however, without influencing its electronic energy levels. As the spacing between rotational energy states of a molecule is relatively small and vibrational quantum number normally varies by only one or two units ($\pm 1$ or $\pm 2$), the corresponding emitted light frequencies are rather small, therefore lying in the near infra-red region.

### 3.2.3. ROTATIONAL ENERGY

Unlike atoms, whenever molecules move, they also rotate. As a result, rotation of the molecules can cause a change in rotational energy. If the change in rotational energy equals the difference between any 2 energy levels (by absorbing or emitting photons), the molecules can transition to a new state, which brings in a new set of energy levels. For simplification, only rigid diatomic molecules are discussed here. The rotational energy of the diatomic molecule about its center of mass can be obtained by classical theory:

$$E_{rotation} = \frac{I\omega^2}{2} = \frac{(I\omega)^2}{2I} = \frac{L^2}{2I}$$

where $I$ is the moment of inertia and $L$ is the angular momentum. Any rigid body has three principal rotational axes. However in this case, the moment of inertia for rotation around the inter-nuclear axis is zero because the molecule is diatomic. Thus, the rotational energy around the inter-nuclear axis is zero, and the
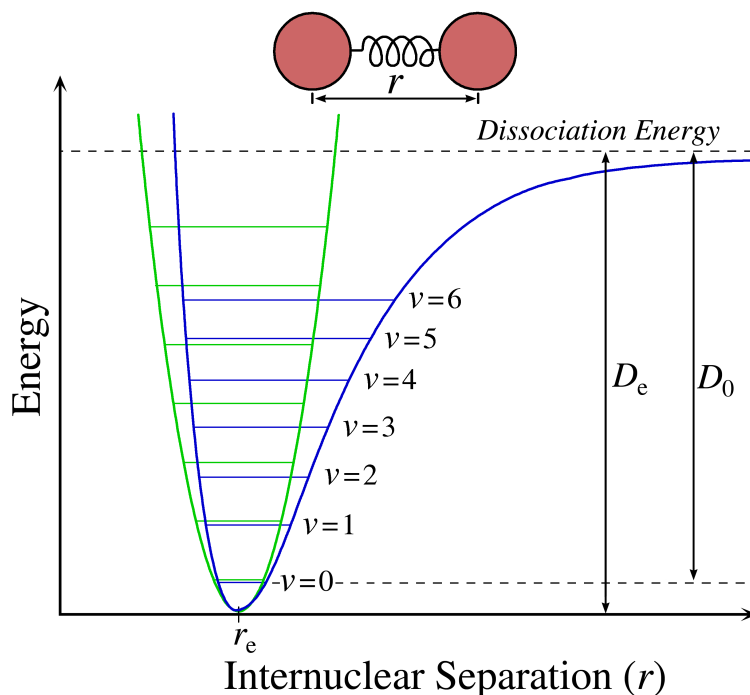
Figure 3.4: The real potential energy curve (blue) for a diatomic molecule compared with the harmonic oscillator approximation curve(green)[1].

diatomic molecules have only two principal rotational axes, both vertical to the inter-nuclear axis, having the same $I$.

From quantum mechanics, the angular momentum, $L$, of the atom is given by:

$$L = \sqrt{l(l+1)}$$

where $l$ is the rotational quantum number which begins with 0 and increases by the increment of 1.

is the reduced Planck constant. In this way the rotational energy can be expressed:

$$E_{rotation} = \frac{L^2}{2I} = \frac{\hbar^2(l+1)l}{2I}$$

Since $I$ and $\hbar$ are all constants, the rotational energy only depends on $l$, which can only take discrete values. Therefore, the rotational energy is also quantized. In pure rotational spectra, the molecule transits from one rotational energy state to another, without influencing its vibrational or electronic energy levels. Since a molecule has the smallest spacing between two rotational energy levels when compared with the other two types of energy and the rotational quantum number $l$ never varies by more than one unit ($\pm 1$), the rotational energy change is very small. In this way, the emitted light frequencies are comparatively small, therefore lying in the microwaves or the far infra-red region.

# 4

# OPTICAL PHYSICS

Combustion diagnostics always requires analysis of the light signal emitted by flames, which is usually collected by a spectrometer. There are 3 optical elements that play a core role in flame emission spectroscopy:

- The optics to collimate the light

- The optics to disperse the light

- The optics to focus the light

The collection of the light is always achieved by a collimator which is usually a converging lens or mirror. The light dispersion is always accomplished by a filter, a prism, or a grating. Light focusing is usually conducted by a converging lens that forms an image on the camera sensor by bringing the incoming light into focus. In summary, only two types of optics will be used in a normal spectrometer, which are converging optics and dispersing optics. In the following two sections, the working principles of them will be elaborated upon.

## 4.1. LENSES AND MIRRORS

Lenses and mirrors are usually used in spectrometers to collimate a light beam, to bring a light beam into focus, and to enlarge or reduce the image size of the object. They may serve more than one of these functions at the same time. For instance, when the light beam is focused on the image plane, the size of the image can be manipulated by selecting converging lenses of different focal lengths.

Since only lenses are available in this thesis project, the features of lenses will be explained in more details and most of the concepts will be explained based on a lens.

### 4.1.1. GENERAL FEATURES OF LENSES AND MIRRORS

In general, depending on whether the transmitted or reflected light is converged or diverged, there are two types of lenses and mirrors:

- Converging (convex) lenses and converging (concave) mirrors.

- Diverging (concave) lenses and diverging (convex) mirrors.

A general example of lenses and mirrors are provided in the figure below to explain some fundamental parameters of lenses and mirrors.

As can be seen from the figure, for a bunch of parallel light rays input, converging (convex) lenses shown in (a) and converging (concave) mirrors shown in (b) are able to make them converge at the focal point of the corresponding lens or mirror. In contrast, diverging (concave) lenses shown in (c) and diverging (convex) mirrors shown in (d) all can cause the light diverge as if they are emanating from the focal point. It is interesting to observe that light rays, after passing through the center of either a converging lens or a diverging lens, does not change its propagation direction.
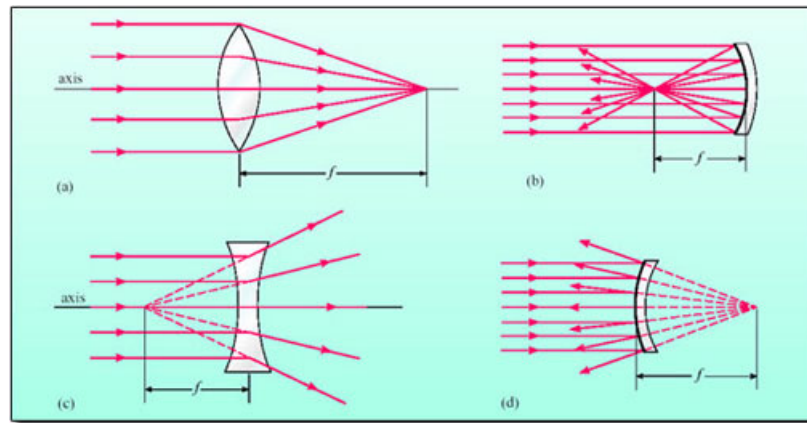
Figure 4.1: An example of lenses and mirrors[2].

Focal point, or focus is a point that locates at a distance of one focal length $f$ from the center of the lens or mirror. Focal point and focal length are two main parameters that characterize the optical performance of lenses and mirrors.

A lens is a transparent device that uses light refraction to change the direction of propagation of light rays, while a mirror is designed to achieve the same task using light reflection.

When light propagates through the boundary between materials of different refractive index, the direction of propagation will be deflected based on the well-known Snell's law. In the case of a lens in the air that has two surfaces along the propagation of light, the light rays will be deflected twice. So one can manipulate the deflection angle by changing the surfaces' curvature, which gives more design possibilities with regard to the converging and diverging characteristics.

In this way, based on the curvature of the lens's surfaces, the converging and diverging lenses can be further divided into a series of subcategories, as shown in the graph below.
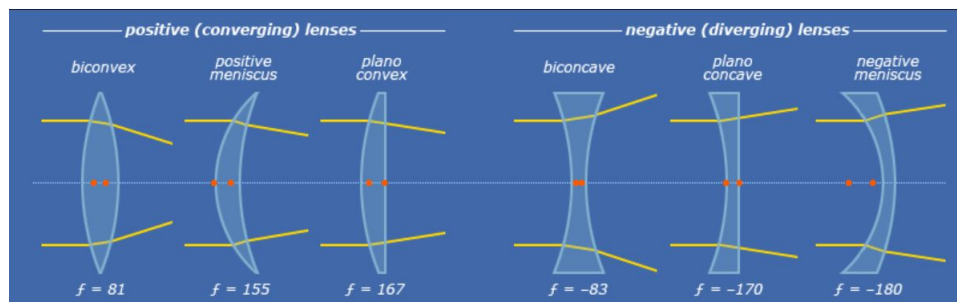


Figure 4.2: An example of the category of lenses[3].

### 4.1.2. Image formation and some commonly used concepts

Before gaining insight into the world of imaging, it is necessary to understand what an image is and how an image is stored in the modern digital world. So the following sections will be concentrated on the basic principles behind imaging. Besides, some commonly mentioned concepts in imaging spectroscopy will also be introduced in this section.

#### Image-forming principles

We are all surrounded by light every day, and it is commonly accepted that why people can see a non-self-luminous object is usually because the light reflected from the object surface is somehow collected by our brains, or, to be more specific, retinas. The function of a retina is like a normal camera sensor or a light screen, which captures the coming light and present the object as a 2D image. If one holds a piece of white paper behind a magnifying glass pointing at a tree outside the window, a clear image of the tree will be formed on the paper at a certain distance, as demonstrated in the left figure below. In this way, a one-to-one mapping is formed. Ideally, each point in the image can be traced back to its corresponding single object point and

each object point has an unique image point. However, if one replaces the magnifying glass with a a piece of plane glass or simply removes the magnifying glass, there will be no image of the tree but only light from outside the window. The light reflected by the tree definitely reaches the paper but why in this case no image is formed? This is because the light from each point of the tree is diverging in this case, as shown in the right figure below. Each point now corresponds to an infinite number of points on the paper, therefore creating an infinitely large blur.



(a) Image is formed
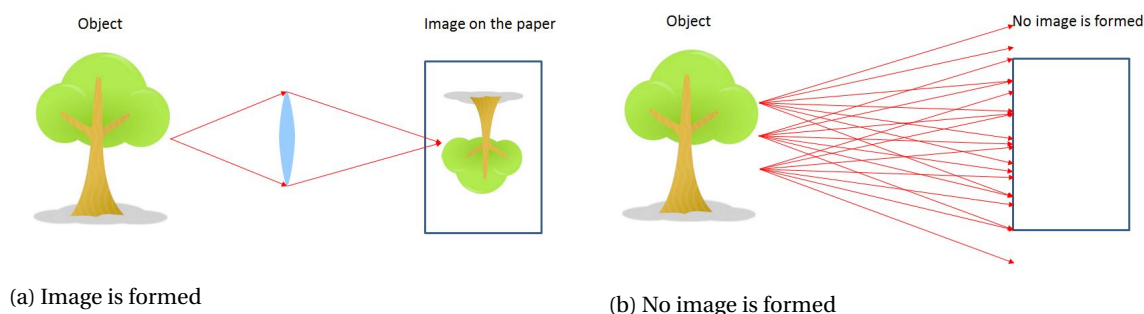
(b) No image is formed

Figure 4.3: A schematic diagram explaining image formation with or without a magnifying glass

In the previous case, the image is formed by focusing the light rays from an object point back to a single point on the image plane. However, one could also think to decrease the number of light rays. The one-to-one mapping will be realized if there is only one light ray left. Imagine that there is an infinitely small pinhole that only allows one light ray to pass through, as illustrated in the left figure below. Only one image point is formed from only one object point, and based on this principle, the pinhole camera is invented. In real cases, as demonstrated in the right image below, the pinhole cannot be infinitely small and when the pinhole size reduces, another phenomenon called diffraction due to the wave behavior of light becomes more remarkable. So the image can also not be infinitely sharp.

Comparing the ability of forming an image, one could find that more light is gathered using a lens, leading to a brighter and clearer image. Therefore, the pinhole is replaced by a lens in most of the fields.



(a) Ideal pinhole camera

(b) Real pinhole camera
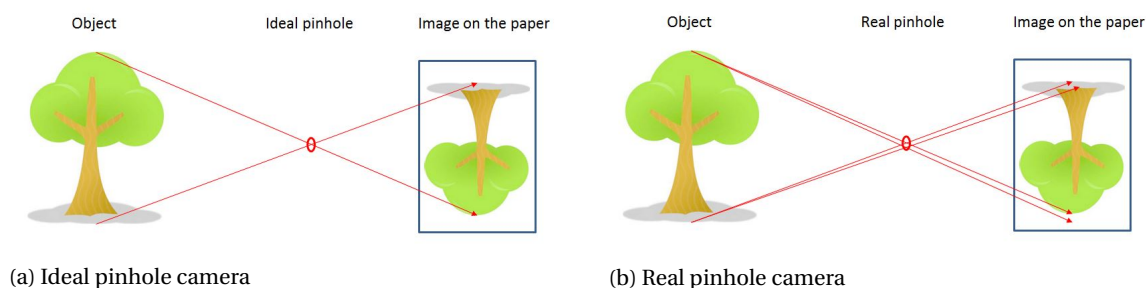
Figure 4.4: A schematic diagram explaining image formation by pinhole cameras.

So one conclusion can be drawn that an ideally sharp image is formed as long as one point in the object plane corresponds to only one point in the image plane. However, in a real imaging system where one object point can not be usually focused perfectly into one image point, the sharpness or resolution of the image always highly depends on how small the corresponding image point area is from a single object point.

### CAMERA SENSORS AND IMAGE STORAGE

Once the image is formed on the image plane, some light receptor, for instance, retinas or camera sensors need to be used to record the image. Presently, there are usually two common image sensors: CCD, which is the abbreviation of charge-coupled device and CMOS, which is the abbreviation of complementary metal-oxide semiconductor. Both of them are constructed from silicon, capturing images by converting incident light (photons) into electronic charge (electrons) through the same photo conversion process. When the light (photons) falls on the image sensor after passing through the lens, they are broken up into the picture elements - pixels. An example is provided here below for the illustration of how the image is pixelated.

Pixels then convert the received number of photons into a corresponding number of electrons. Always, a stronger light or in another word a larger amount of photons means that more electrons are generated in this process. After the photon-to-electron conversion is complete, the converted electrons are then converted into voltage, after which they are transformed into a string of binary numbers by means of an A/D-converter. Finally, the signal represented by the numbers is processed by electronic circuits inside a camera. For a grey-scale image, each number in a pixel indicates the intensity recorded in this pixel, telling how bright or dark the picture element is, as explained in the figure below. If all the pixels possess the same intensity value, the image will a uniform color base, pure black, grey or white.
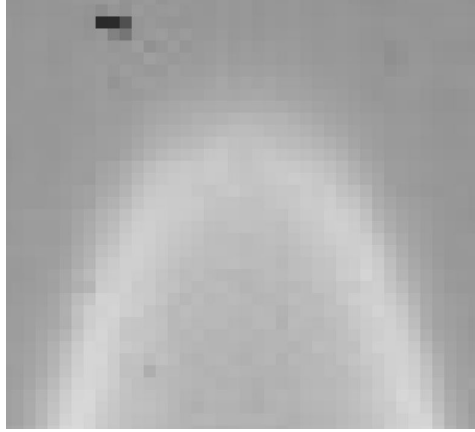


Figure 4.5: A zoomed-in view at the Bunsen flame tip. The picture is actually pixelated and the pixels can be seen as multiple small squares, each of which stores the intensity information of the corresponding picture element.
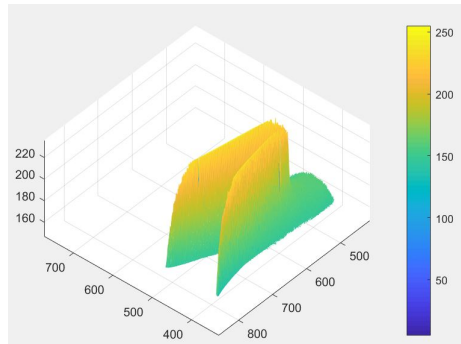


Figure 4.6: A zoomed-in 3D surface plot of the Bunsen flame reaction zone using Matlab. The color bar tells the surface height, which is the intensity in this case. It is obvious that the tip of the flame has less brightness compared with adjacent part of the reaction zone.

There are also some main differences between the two image sensors. Unlike a CCD sensor, a CMOS sensor itself includes amplifiers, A/D-converters and normally circuity for extra signal processing, in this way, increasing the readout speed while decreasing the price and system size. Nevertheless in a camera that uses CCD sensor, multiple functions of signal processing are conducted outside the sensor, which makes it slower and expensive. However, due to the compactness of CMOS sensors, they also tend to have lower image quality, lower light sensitivity and more image noise.

A CCD sensor normally consumes up to 100 times more power than an equivalent CMOS sensor[35]. It therefore results in a way higher temperature inside a CCD camera in comparison to a CMOS camera. For CCD sensors, the overheating problem caused by excessive power consumption may lead to a higher thermal noise of the pictures. However on the other hand, CMOS sensors also tend to have more structured noise due to the addition of circuitry inside this chip.

In summary, CCD sensors tend to be used in the situations that require high image quality, low light operations and high precision measurement such as flame emission spectroscopy in this project while the CMOS sensors are more suitable for the situations that require high readout speed and low power consumption, sometimes at the cost of lower image quality. Please also keep in mind, today the CMOS sensor is becoming more and more popular not only because of its advantages mentioned before but also because that the

original advantages of CCD sensors as mentioned above such as higher light sensitivity and less noise have gradually disappeared due to the recent technology advancements of CMOS sensors.

### TWO EQUATIONS OF MIRRORS AND LENSES

The first equation is also called spherical mirror equation or thin lens equation, meaning that it is applicable to a spherical mirror or a single thin lens. This approximation is convenient to use since it provides a simple relation between object distance $d_o$, image distance $d_i$, and focal length $f$ :

$$\frac{1}{d_o} + \frac{1}{d_i} = \frac{1}{f}$$

where the object distance $d_o$ is defined to be the distance of an object from the center of a lens or a mirror and the image distance $d_i$ is defined as the distance of the image from the center of a lens or a mirror.

$f$ is positive for category 1: converging (convex) lenses and converging (concave) mirrors, negative for category 2: diverging (concave) lenses and diverging (convex) mirrors. The object distance $d_o$ is positive when the object is in front of the optical system, negative when behind it. For the image distance $d_i$, it is positive when a real image is formed (behind the lens and in front of the mirror), however it becomes negative when the image is virtual (in front of the lens and behind the mirror).

This approximation turns out to be quite accurate with the currently available lenses in the lab, therefore the initial setup could be based on this relation.

The second equation is called magnification equation. The magnification factor $m$ in $2D$ is defined as the ratio between the image height $h_i$ and object height $h_o$, which is also related to $d_o$ and $d_i$ because of the similar triangles:

$$m = \frac{h_i}{h_o} = -\frac{d_i}{d_o}$$

The magnification factor $m$ indicates that how large or small the image is with respect to the object. It is positive if the image is a real image, which is upright ($h_i$ positive and $d_i$ is negative) and negative if the image is a virtual image, which is upside down ($h_i$ is negative and $d_i$ is positive).

An example is provided below for a more intuitive understanding of the object-to-image relation.
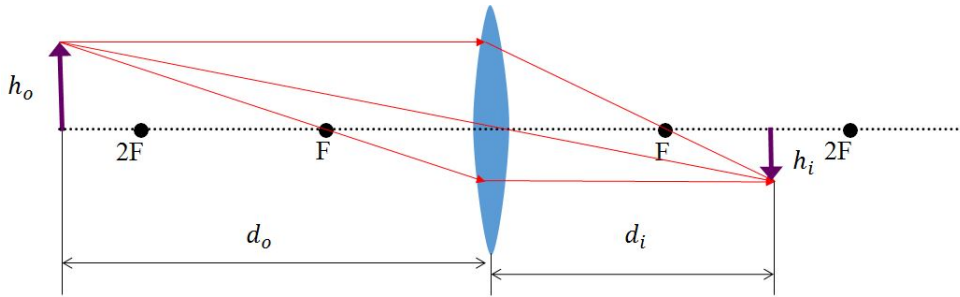


Figure 4.7: An inverted and scale-down image is formed if the object distance is greater than 2 times of the focal length.

### NUMERICAL APERTURE AND $f$ NUMBER

Numerical Aperture (NA) is originally defined to describe the acceptance cone of microscope objectives by Abbe, which is always placed at one focal length away from the specimen[36]:

$$NA = n\sin\theta$$

Where $n$ is the refractive index of the medium between the object (specimen) and the front of the lens, which is 1 for air, and $\theta$ is the maximal half-angle of the cone of light, as shown below. It tells how much light from the object can be captured by the objective lens. Larger $\theta$ always means larger portion of the spherical light wave from the object can be captured, resulting in a higher resolving power and thus finer details of the object can be visualized.

The author realizes that this definition is also convenient to use in spectroscopy since, for the collimating lens, the distance between the object and the lens is also one focal length $f$. In addition to numerical aperture, another similar concept f-number (f/#), widely used in photography, turns out to be also expedient to

describe the ability of capturing light in spectroscopy, which is defined in the formula below. This number is always written in camera lenses and the value can be changed by opening or closing the physical aperture in a camera lens.

$$f/\# = \frac{f}{D}$$
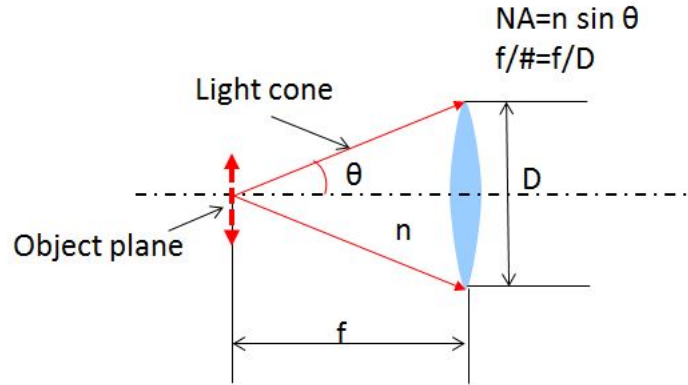


Figure 4.8: Numerical aperture and f number.

### 4.1.3. COMMON LENS ABERRATIONS IN SPECTROSCOPY

Ideally, light from any point of the object will be focused to a single point in a flat image plane. However, due to the imperfections in the imaging system, the light is always spread out spatially, meaning that one point in the object now corresponds to multiple points in the image plane or the original spatial distance is magnified non-uniformly along the optical surfaces, which causes the image blurred or distorted.

The lens aberrations are usually composed of chromatic aberration, spherical aberration, coma, distortion, curvature of field, and astigmatism.

Among them, according to the research of William Schrenk, there are three aberrations in lenses that are important in their use in spectroscopy, which are[7]:

- Chromatic aberration

- Spherical aberration

- Coma

The first two defects belong to on-axis aberration because they occur along the optical axis. Whereas the third defect is an off-axis aberration, since this defect is caused by oblique illumination.

In addition, the author also finds a type of astigmatism: off-axis astigmatism (due to oblique illumination) always bundled with coma, which can also be added to the aberration list.

- Astigmatism

According to the author's research in flame emission spectroscopy, when it comes to flame imaging, the other 2 aberrations are also commonly noticed, which are:

- Distortion

- Curvature of field

Moreover, another optical defect: anamorphic magnification caused by diffraction grating also plays an important role especially in imaging spectroscopy, which will be explained in the section of diffraction grating.

In the following subsections, the 6 aberrations mentioned above will be explained and identified using the available optics in the lab.

### CHROMATIC ABERRATION

Chromatic aberration occurs because different colors of light (wavelengths) have different indexes of refraction regarding a lens. As a result, all colors do not focus at the same focal point, as shown in the left photo in the figure below. Chromatic aberration can be minimized by use of compound lenses, made of two or more different glasses, with different indices of refraction, cemented together[7]. The right photo provides an example of the achromatic lenses.
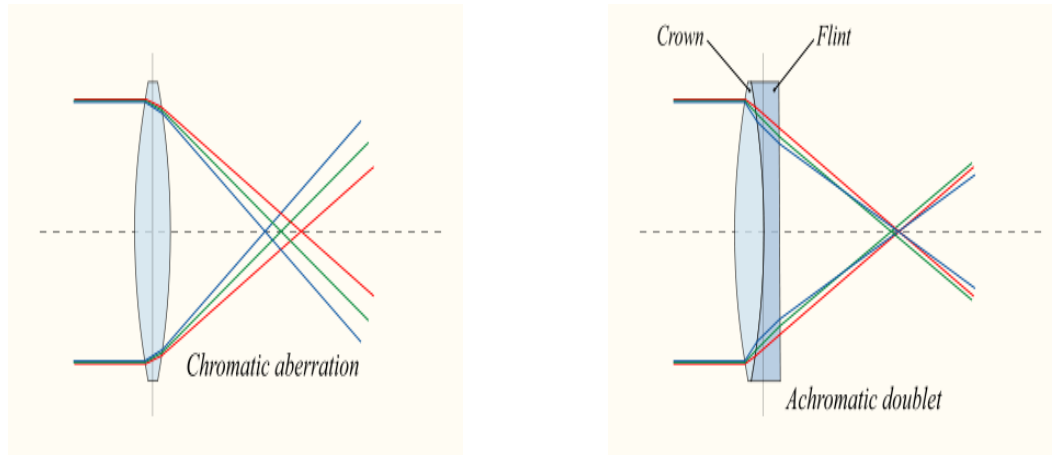


(a) Chromatic aberration                          (b) An achromatic lens design

Figure 4.9: Chromatic aberration and achromatic lenses [4].

A comparison is made using a 200mm normal lens and the 200mm achromatic lens, as shown in the figure below. Both lenses are positioned at 200mm away from the white LED light source. The outer rim is slightly reddish in figure(a) due to chromatic aberration.
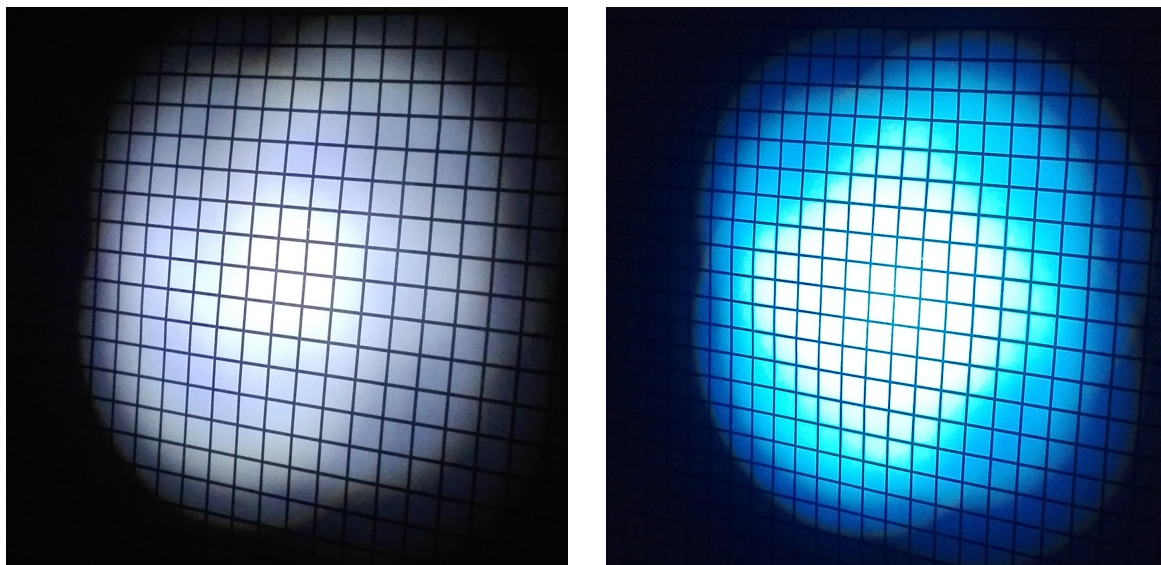


(a) 200mm normal lens                             (b) 200mm achromatic lens

Figure 4.10: Chromatic aberration identification

## SPHERICAL ABERRATION

Spherical aberration happens when all incoming light rays are focused at different points after passing through various parts of the lens. Light rays passing through a lens close to the center of the lens are refracted less than rays near the edge of the lens and in this way, they are focused in different spots along the optical axis, as can be seen in the figure below. This effect can be serious and for use in spectrometers it frequently requires correction[7].

Spherical aberration is possible to be reduced by two approaches. The first approach is to use only the central part of the lens, however this method also reduces the light-gathering power of the lens. Secondly, the lens shape can be manipulated for having the same index of refraction in all parts. It is achieved by employing a specially-designed apsherical lens surface that curves outwards in the center, as illustrated in the figure below. However this approach increases the difficulty of producing a lens, and consequently, the manipulated lenses are much more expensive.



(a) Spherical aberration                              (b) An ashperical lens design
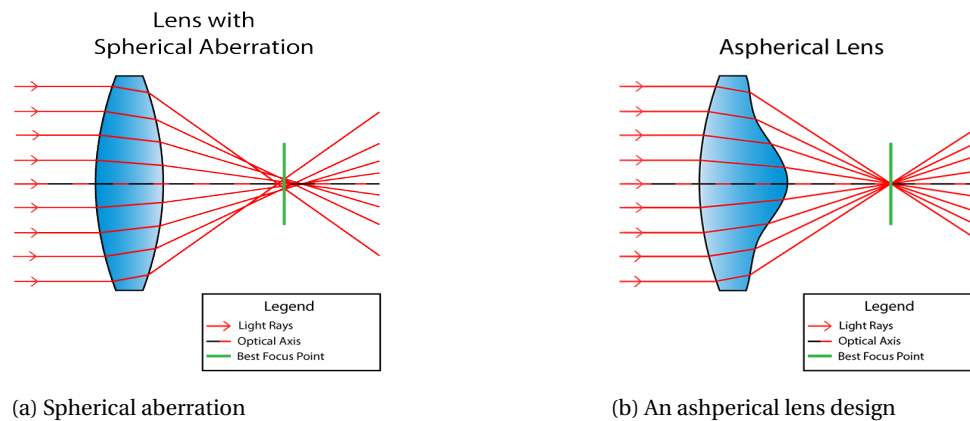
Figure 4.11: Spherical aberration and apsherical lenses [5].

There is no ashperical lens available in the lab currently, so the spherical aberration identification is conducted using a 100mm plano-convex lens based on the principle that there is more spherical aberration if the plano surface faces the collimated light. In this test, the 692nm HeNe laser is used as the light source, which is firstly collimated and then refocused by the plano-convex configuration (figure(a))and the convex-plano configuration(figure(b)).

The camera sensor is positioned somewhere before the focal plane for increasing the difference in results and the diameter of the beam in camera sensor is used to identify this aberration. Due to the more severer spherical aberration in the plano-convex configuration (figure(b)), the beam appears to be larger.



(a) Convex-plano configuration                       (b) Plano-convex configuration
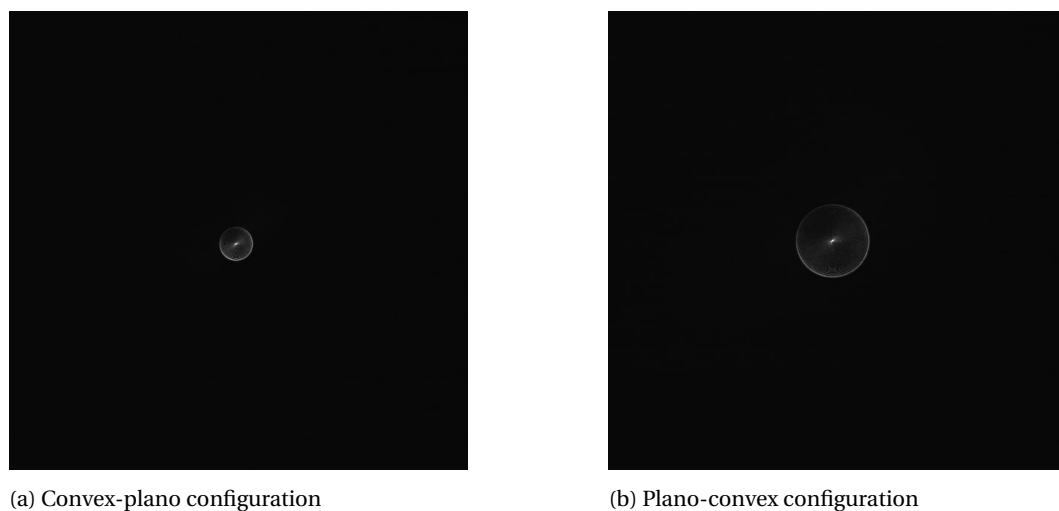
Figure 4.12: Spherical aberration identification

COMA AND ASTIGMATISM

Coma, or comatic aberration happens when light rays passes through the lens at an oblique angle, as is illustrated in the Figure below. When the incoming parallel light rays pass through the lens at an angle, individual rays are not refracted to the same point due to the different refraction of light along the lens. The light rays near the edge have a relatively longer focal length in this case and thus are focused behind the image plane, creating a blur.

The coma appears to have a tail (coma) like a comet with a tail. The effect may be most noticeable in a collimating lens[7]. In order to reduce this defect, lenses should be mounted in a way that allows light to enter the lens along the optical axis if at all possible[7]. Beside aligning the incoming light, coma can also be reduced by using a smaller central part of the lens, however resulting in reduced light intensity as a negative side effect.
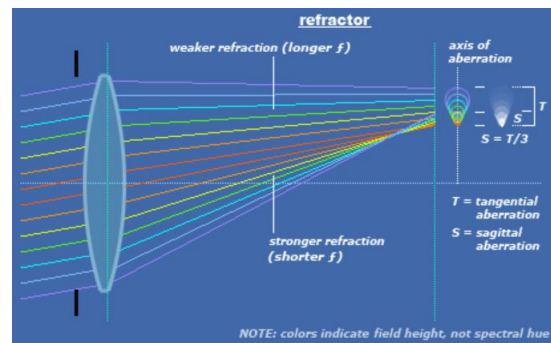


Figure 4.13: A demonstration of comatic aberration[3].

Astigmatism is a phenomenon that different light propagation planes have different foci, which results from:

1. Non-rotationally-symmetrical lens shape

2. Off-axis illumination

The first form of astigmatism is due to the different lens curvatures for different light propagation planes. If the curvatures of some planes are larger than that of the others, the light rays will be converged faster, resulting a shorter focal length.

This type of astigmatism only happens in lenses that are not rotationally symmetrical, which is not encountered in the thesis project because all the lenses used in the experiment have perfectly symmetrical circular shape.

The second form of astigmatism is caused by different incidence angles for different light propagation planes. As illustrated in the figure below, the off-axis illumination creates two different incidence angles for the tangential plane and the sagittal plane, leading to two different foci and therefore two different resolutions in the image plane.

This type of astigmatism is commonly seen in the thesis project. If the incoming collimated light is somewhat off-axis, the resulting geometry on the image plane will be slightly skewed, as can be seen in the identification result.

This comatic aberration is always bundled with off-axis astigmatism, as shown in the figure below. The 100mm lens is illuminated obliquely with collimating light (692mm HeNe laser) and the camera sensor is slightly in front of the focal point in order to increase the difference in results. The tail can be obviously noticed and the oval shape due to off-axis astigmatism is also significant (the light rays from the tangential plane converge before that of the sagittal plane).
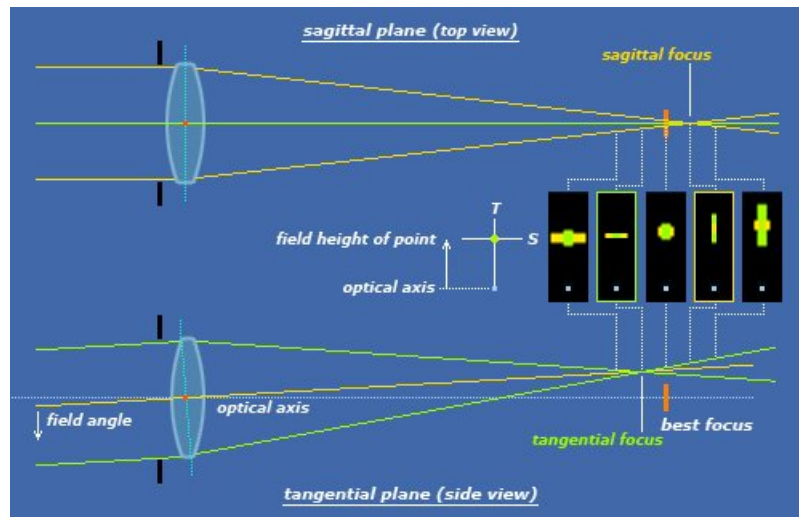
Figure 4.14: A demonstration of off-axis astigmatism [3].
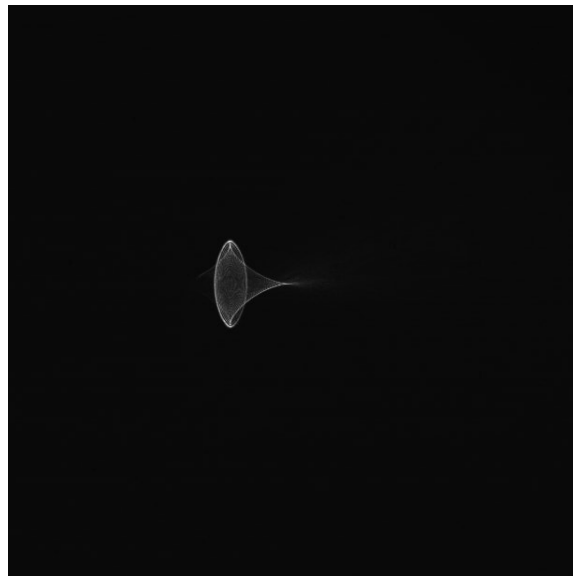


Figure 4.15: Coma and off-axis astigmatism identification.

### DISTORTION

Served as a type of lens aberration, distortion is described as the deviation from rectilinear projection, where the expected straight lines appear to be curvy or having a different aspect ratio in an image[6]. Distortion can be further divided into two types: Optical distortion and perspective distortion, which will be explained in the following paragraphs.

### • OPTICAL DISTORTION

As the term indicates, optical distortion is only caused by the uneven magnification of the optical design itself of a lens with the most encountered type being radially symmetric due to the radial symmetry of common lenses[6].

These radial distortions usually can be categorized as two types: barrel distortion or pincushion distortion. In barrel distortion, the magnification of the image increases radially towards the edge of the image. However the magnification in pincushion distortion decreases radially towards the edge of the image, as demonstrated in the following figure.

(a) Barrel distortion

(b) Pincushion distortion
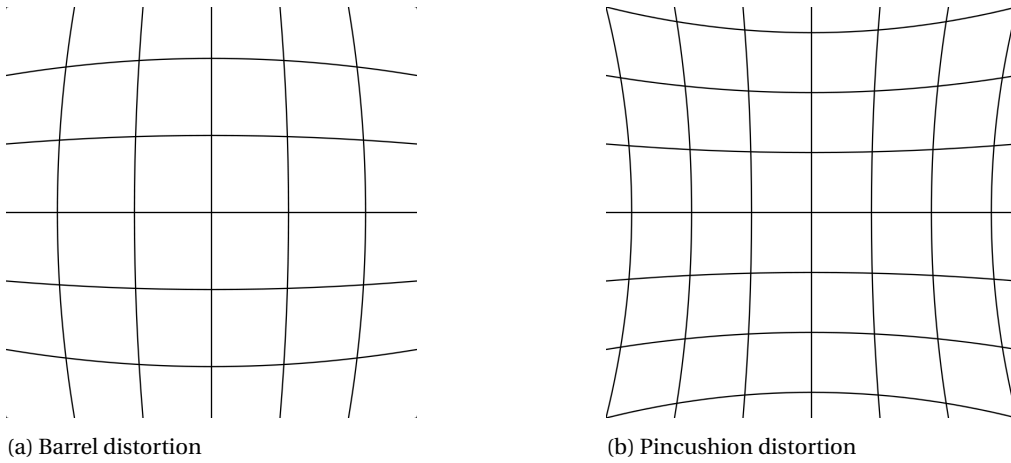
Figure 4.16: Two types of commonly seen optical distortions[6]

Fortunately, the author does not find a visible optical distortion by naked eyes in his setup, as shown in the picture below.
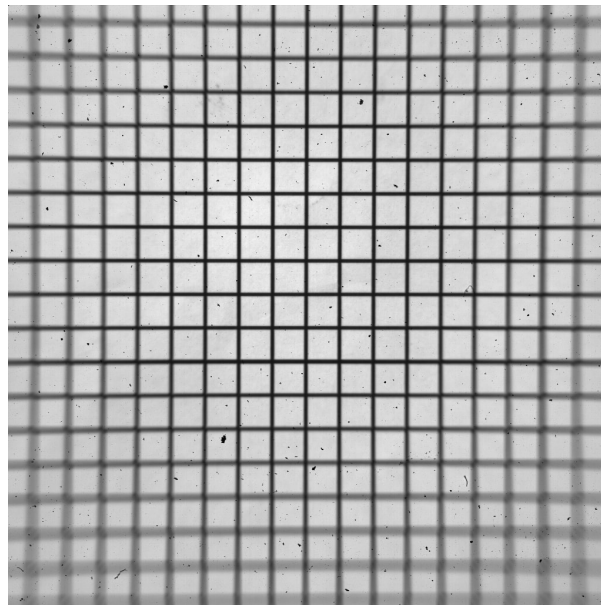


Figure 4.17: Optical distortion test of the experimental setup. No visible distortion can be found, regardless of the curvature of field, the lines in the central part of the image are straight.

• PERSPECTIVE DISTORTION

The other type of distortion is called perspective distortion, which is caused by the nonparallel alignment between the camera or camera sensor and the object plane, as explained in the diagram below.
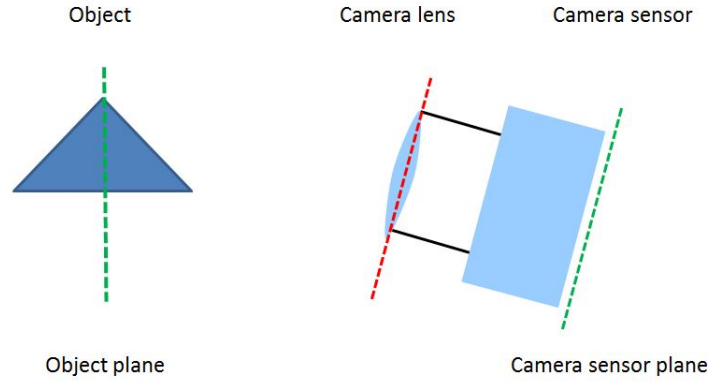


Figure 4.18: Perspective distortion. The object plane is not parallel to the camera sensor plane. The bottom of the object is now closer to the camera sensor, creating a larger magnification when compared with the tip of the object.

This distortion happens quite often especially in imaging spectrometer. Because firstly, for the normal imaging process without the spectral imaging involved, there is always some misalignment between the object plane and the camera sensor, which is the source of perspective distortion. Secondly, in addition to the normal perspective distortion, for an imaging spectrometer, after the dispersion of the light, the light of different wavelengths has different exit angles, making the current planar camera sensor unable to be aligned with all the wavelengths simultaneously.

Fortunately, according to the author's research, due to the relatively small object, the imaging spectrometer used in this project is not very sensitive to this type of distortion, as shown in the figure below. An obvious difference in the vertex angle of the right triangle can only be seen at a relatively large tilt angle, which means that the second source of perspective distortion mentioned above may be negligible for adjacent spectral peaks. The right photo has a tilt angle relative to the camera sensor around 30 degrees.
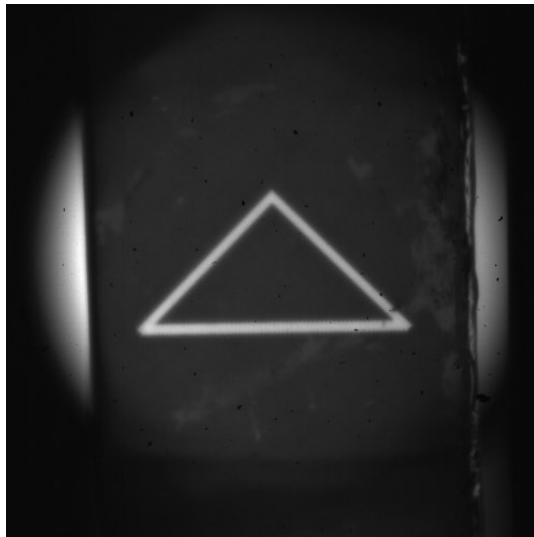


(a) Target parallel to the camera sensor                    (b) Target nonparallel to the camera sensor
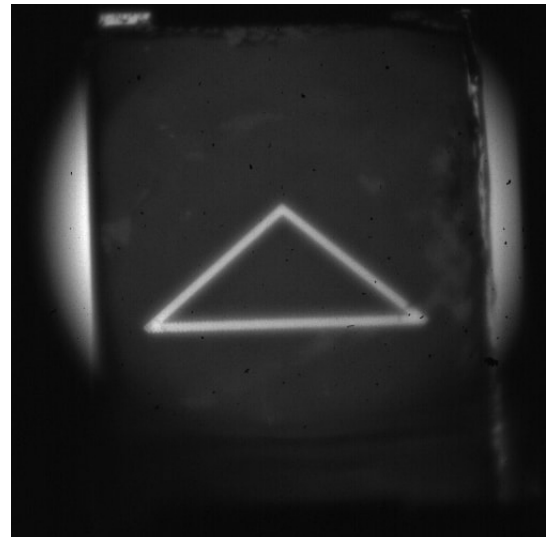
Figure 4.19: Perspective distortion tested using the experimental setup.

### CURVATURE OF FIELD

Curvature of field or Petzval curvature is a failure to focus the entire object in a flat object plane perpendicular to the optical axis into a flat image plane[3]. Instead, the image plane becomes curved, resembling a bowl or meniscus, as demonstrated below. As can be noticed in the figure, this type of aberration is highly related to astigmatism. The light rays that are not normal to the lens axis have a different focal length, either shorter(positive curvature) or longer(negative curvature).
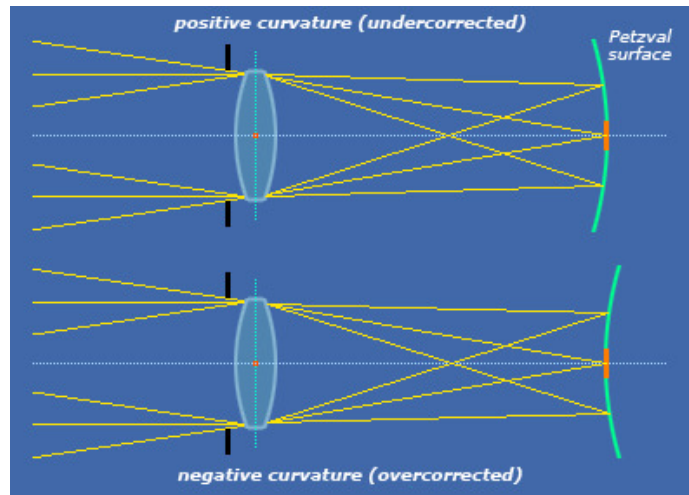


Figure 4.20: A demonstration of off-axis astigmatism [3].

The author finds that in imaging spectroscopy curvature of field is strongly dependent on the collimating lens. A better collimation always leads to less curvature of field, as can be seen in the figure below. Since the central part of the grid target is better collimated than the marginal part, the curvature of field for this central region is also less and thus it can be imaged on a relatively flat surface.
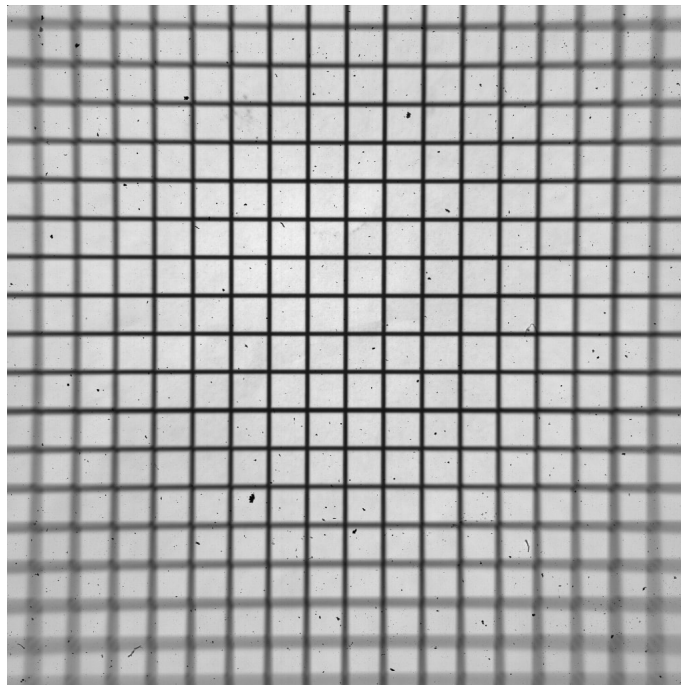


Figure 4.21: A positive curvature of field is found using the experimental setup. The central part of the image is sharper due to less curvature of field.

### 4.1.4. THE COLLIMATOR

#### THE EXPLANATION OF COLLIMATION

One of the major functions of lenses and mirrors in spectroscopy is light collimation, which is a concept always used for a point light source, meaning parallelizing incidence light rays. Since all real sources have a finite size, i.e., no object is actually a point, there is no light source, no matter how small it is, that can be really collimated. So in order to expand the usage of this concept, most of time for a collimating lens, this concept is applied to every individual point in the object. So one can say that the light source is collimated if it is at the focal point of the collimating lens, forming an image at infinity. The term "collimation" used in this thesis is all based on this explanation. The objects are all positioned at the focal point of the collimator and better collimation only means that the light rays after passing through the collimator are more parallized.

#### THE EXPERIMENTAL STUDY OF COLLIMATION

According to the definition given in the last paragraph. The light rays will all be collimated as long as the object is at the focal point of the collimator. However, collimation does not mean parallelism. Better collimation or higher parallelism of light rays is beneficial to reduce the lens aberration, as discussed before. In order to study the influence of the focal length of a collimating lens on the result of collimation, an experiment is designed as shown in the figure below.
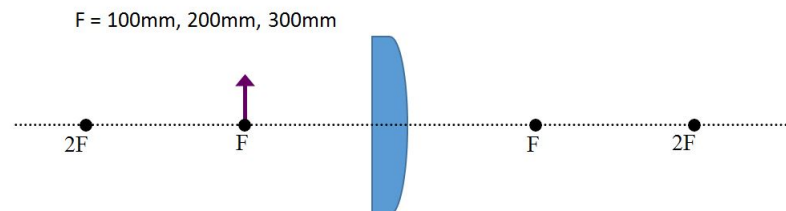


Figure 4.22: The schematic diagram of the collimation test
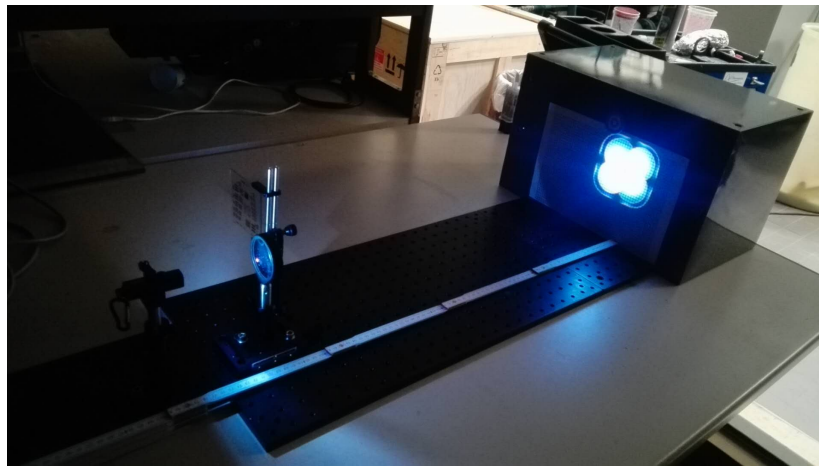


Figure 4.23: The experimental setup of the collimation test. The size of the object is about 1.4cm long and 1.4 cm wide. The diameter of the lens is 5cm. The grid screen locates at about 70cm behind the converging lens.

3 plano-convex lenses of 3 different focal lengths 100mm ,200mm, and 300mm are tested. The object, a flashlight with 4 LED light bulbs, is placed at one focal length away from the 3 lenses separately, so that the light emitting from the object is collimated and the image is formed at infinity. The collimation then is quantified by the diameter of the light projected on a piece of grid paper at around 70cm behind the lens. If the light is totally collimated (an ideal point source), the projection on the paper will be a circle that has a diameter of 5cm.

The result shows that, as the focal length increases from 100mm to 300mm, the diameter of the projection on the grid paper is decreasing, as shown in the figure below. The parallel light output is almost achieved for the 300mm lens within a distance of 70cm. However since the numerical aperture is decreasing from 100mm to 300mm, the brightness of the projection is also reducing.
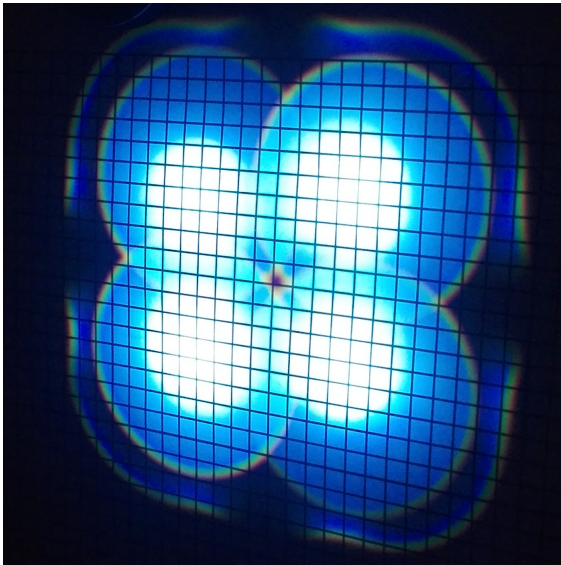


(a) $f = 100mm$
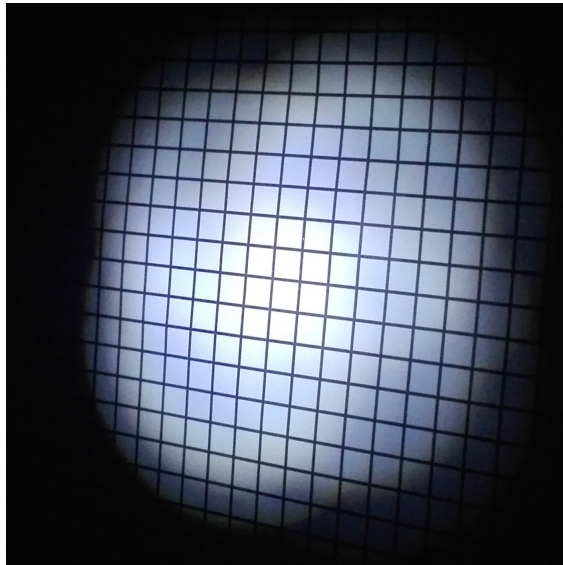


(b) $f = 200mm$
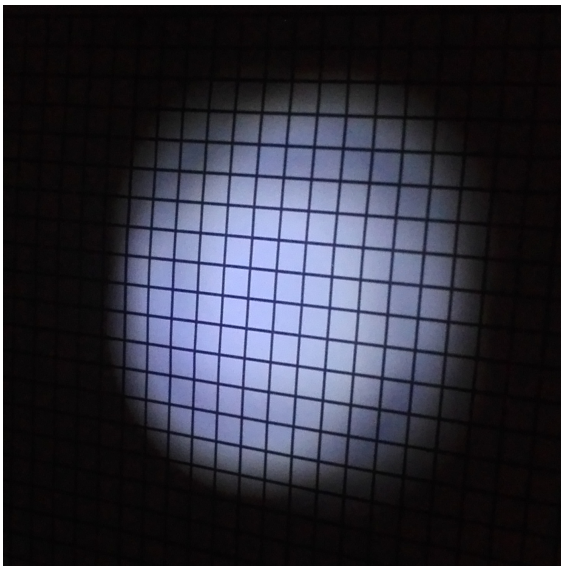


(c) $f = 300mm$

Figure 4.24: The collimation test with 3 plano-convex lenses of different focal lengths.

Most of the well-known classical spectrometric instruments (such as filters, prisms and diffraction gratings) require parallel light output, in another word, the image formed at infinity [37]. The greatest resolution will be achieved if the dispersing element is illuminated with collimated light or in another word plane light waves[32]. Although there are some rare cases that non-collimated light is used when the light source is very faint and the resolution is not of prime importance[38]. In most situations, it is essential that the incidence light rays on the dispersing element are collimated, which is achieved by positioning the object at the focal point of the collimator.

The collimator is considered as an optical subsystem, usually made up of an aperture that is relatively small compared to the collimator and an image forming element (lens or mirror) which is used to form the image of the aperture usually at infinity. The aperture is located at the front focal point of the image forming element, after which the light coming from the aperture is collimated.

The entrance slit commonly has a rectangular shape with the longer side normal to the plane of dispersion. Because of light diffraction, there is a constraint for minimum slit width which can be approximately calculated by the Rayleigh criterion[37]. In this way, the resolution of the spectrometer is not affected by the collimator slit width. As long as the entrance slit is considered small when compared with the image forming element, it can be approximated as a point source along the plane of dispersion, in this way, the lens aberrations in this plane caused by off-axis light rays will be of little concern[37]. Distortion and curvature of field may also be neglected. The aperture can also be absent sometimes for a slitless spectrometer, which means that the image forming element alone works as the collimator.

The image forming element is normally a single lens or a curved mirror. For a light source that has a weak radiance such as a Bunsen flame, it becomes more important to increase the light capturing capability of the image forming element. Besides using an objective of larger numerical aperture, increasing the transmission or reflection rate for the spectral region of interest also offers a good solution. Compared with lenses made from glasses, curved mirrors frequently have a better light capturing capability for the spectrum in middle and short wavelength UV region, which is the main interest of analytical work[37]. In addition to this advantage, since the reflection of light is not wavelength-dependent, curved mirrors are also free of chromatic aberration.

## 4.2. The dispersing system
In order to analyze the desired spectral region, the light has to be usually dispersed by a filter, a prism, or a grating. Which dispersing element to use depends on the spectral region of interest and the degree of wavelength resolution required. The following sections will discuss about the features and working principles of these three dispersing elements. More attention will be paid on diffraction gratings, since currently there are only diffraction gratings available in the lab.

### 4.2.1. The filter
Color filter and interference filter are the two most commonly available filters today. The three main requirements of a filter are[7]:

1. High transmission rate in the desired wavelength region.

2. Low transmission rate at all other wavelengths.

3. A narrow wavelength band in the high-transmittance region.

The simplest device that is used to isolate a spectral region is a color filter. Commonly used colored filters consist of colored glass, colored films, or solutions of colored substances[7]. The most appropriate color filter is the one with its maximum transmission at the desired wavelength and a small spectral bandwidth measured at a transmittance of one-half the maximum, as shown in the figure below.

However a color filter usually has relatively wide bandwidth, which are 35 to 40 $nm$. It is therefore necessary to combine colored substances to produce a suitable filter for narrowing down the spectral bandwidth.

The other type of filter is interference filter. Compared with a color filter, it can provide better spectral isolation. The bandwidth measured at a transmittance of one-half the maximum may be as low as 10 $nm$. Just as the name implies, the working principle of interference filter is based on light interference. The filter itself is made up of two parallel, half-silvered (semitransparent) surfaces $I$ and $J$, carefully spaced by a transparent material, as shown in figure the figure below. In order to have the reflected light $DE$ interferes with the transmitted light ray entering at $E$, the space between surfaces $I$ and $J$ is designed to be one-half of the
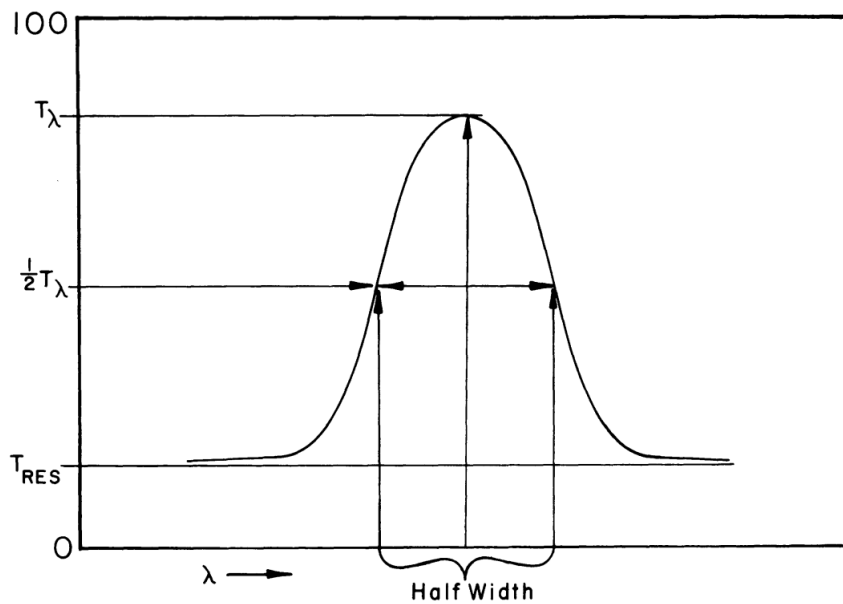
Figure 4.25: Characteristics of a color filter[7].

desired wavelength. In this way, the path difference $CD + DE$ becomes exactly one wave length $\lambda$, so the light of wavelength $\lambda$ will be reinforced and emerge from the filter.

It should be reminded that the interference filter is always used with the incident light beam perpendicular to the filter surface. Here, in order to illustrate the principle clearer, the entering beam is drawn oblique to the filter.

Frequencies harmonically related to the fundamental frequency $\lambda$ of the interference filter will also be reinforced. If these harmonically related frequencies are a source of difficulty in the use of the interference filter, they can be removed by combining the interference filter with a color filter with peak transmittance at the same wavelength as the fundamental of the interference filter[7].
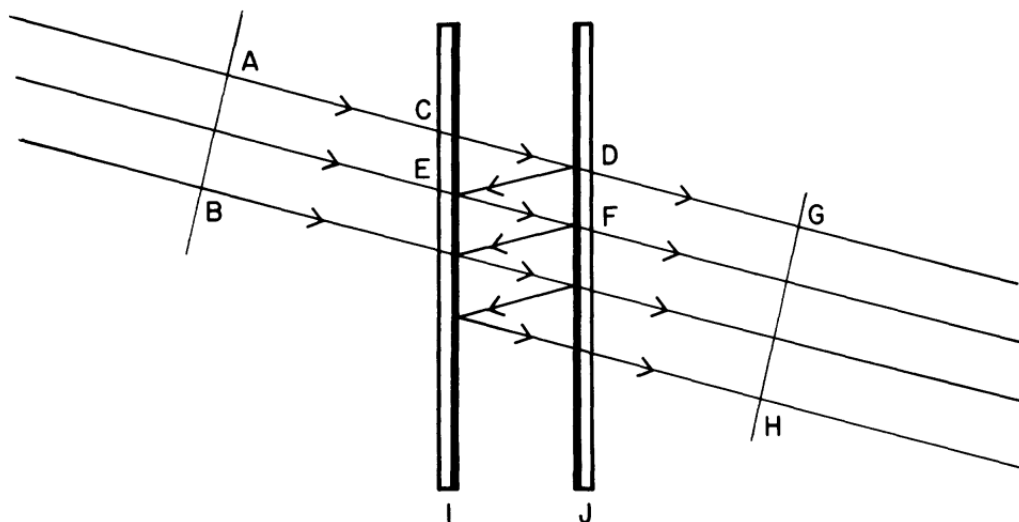


Figure 4.26: Light path through an interference filter[7].

## 4.2.2. THE PRISM

A prism designed for spectroscopy is called a dispersing prism, which is used to disperse incoming light into its constituent colors or to be more specific wavelengths because the refractive index and thus deflection angle is different for different wavelengths.

It is based on the theory of refraction of light, which is formulated by Snell (1620). As light propagates from one medium to a new medium of different refractive factor $n$, the speed of light changes. This speed change leads to refraction of light rays so that they enter the new medium at different angles. Thus in the case of a prism, light is usually deflected twice on the two interfaces. The diagram below shows how the white light is dispersed in a prism.
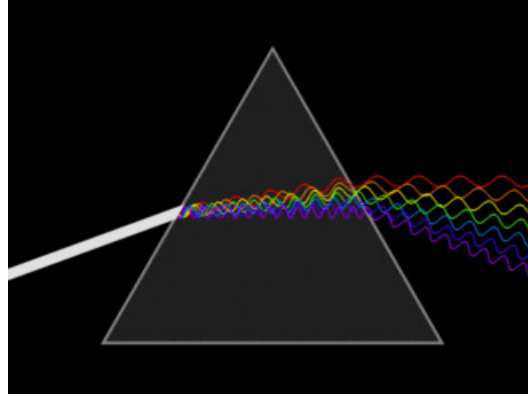


Figure 4.27: White light dispersion through a prism[8].

As stated by Snell's law, the ratio between the sine of the incidence angles in $i$ to the sine of the refraction angles in $r$ is constant $n$. The refractive index n is a property of the substance involved and it is also a function of wavelength. In another word, different materials have different refractive index $n$ for the same wavelength and the same material also have different refractive index $n$ for different wavelengths. The refractive index $n$ is also the ratio between the speed of light in a vacuum $c$ to the speed of light in a denser medium $v$. Therefore Snell's law becomes:

$$\frac{\sin i}{\sin r} = n = \frac{c}{v}$$

### DISPERSION OF A PRISM

The angular dispersion $\frac{d\theta}{d\lambda}$ is defined as the rate of change in deflection angle $d\theta$ divided by the change in wavelength $d\lambda$.

Figure below illustrates the light path of a monochromatic beam of light through a prism at the angle of minimum deviation, which is realized by modifying the incidence angle till the light beam inside the prism is parallel to the base of the prism. If the incidence light beam in this case moves either upward or downward, the deviation angle $\theta$ of the light will be greater.

The angular dispersion of the prism can be written as:

$$\frac{d\theta}{d\lambda} = \frac{d\theta}{dn}\frac{dn}{d\lambda}$$

It is easy to derive that $A = r_1 + r_2$ and $\theta = d_1 + d_2 = i_1 - r_1 + i_2 - r_2$ at minimum deviation. Combine them, the following equation can be obtained:

$$\theta = 2i - A$$

Therefore, Snell's law can be expressed as:

$$n = \frac{sin(i)}{sin(r)} = \frac{sin[(\theta + A)/2]}{sin(A/2)}$$
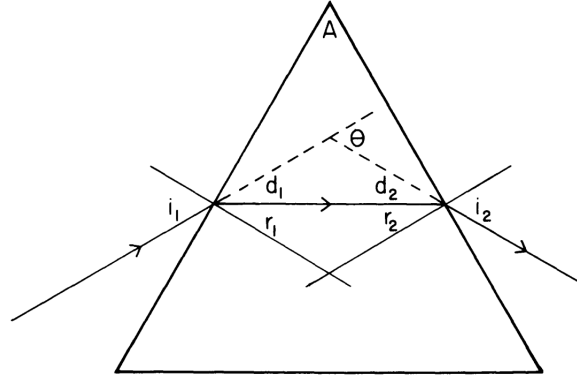
Figure 4.28: The path of monochromatic Light through a prism at minimum deviation[7].

So that:

$$\frac{d\theta}{dn} = \frac{2sin(A/2)}{cos[(\theta+A)/2]} = \frac{2sin(A/2)}{[1-sin^2(\frac{(\theta+A)}{2})]^{\frac{1}{2}}} = \frac{2sin(A/2)}{[1-n^2sin^2(\frac{A}{2})]^{\frac{1}{2}}}$$

Hartmann gives an empirical formula that relates refractive index and wavelength[7]:

$$n = n_0 + \frac{c}{\lambda - \lambda_0}$$

So that:

$$\frac{dn}{d\lambda} = \frac{c}{(\lambda - \lambda_0)^2}$$

Therefore, the final equation for the angular dispersion of a prism as the wavelength changes is:

$$\frac{d\theta}{d\lambda} = \frac{2csin(A/2)}{(\lambda - \lambda_0)^2[1-n^2sin^2(\frac{A}{2})]^{\frac{1}{2}}}$$

As can be found in the equation, the angular dispersion decreases as the wavelength increases. This explains why the angular dispersion for red light is less than that for a violet light in a prism.

### RESOLVING POWER OF A PRISM

The resolving power is generally defined by the expression: $R = \frac{\lambda}{d\lambda}$. It signifies the ability of the prism or grating to just resolve two neighboring lines near wavelength $\lambda$ with a separation of $d\lambda$.

The criterion used by Lord Rayleigh is most generally accepted for this purpose, which states that two lines could be resolved if the minimum intensity of one line is just below the maximum of the line near it. As demonstrated in the figure below, the middle figure is resolvable. The minimum intensity of the left pattern is just below the maximum intensity of the right pattern.
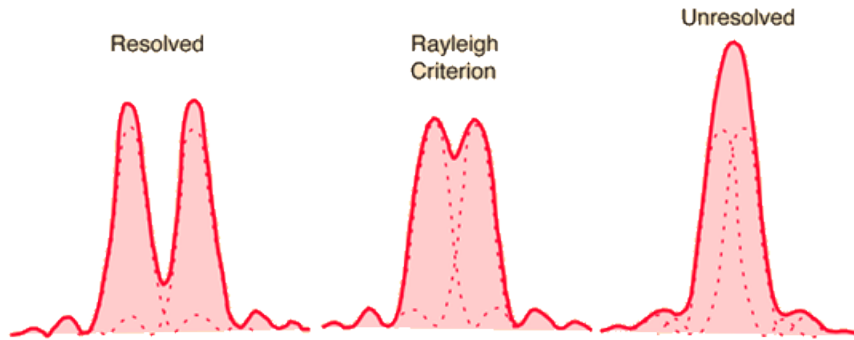


Figure 4.29: Rayleigh criterion[9].

For a prism, the theoretical resolving power can be deduced:

$$R = b\frac{dn}{d\lambda}$$

Where b is the base of the prism, $\frac{dn}{d\lambda}$ is a property of the prism material itself. The deduction of this formula can be found in the textbook of Schrenk[7].

The expression is only applicable for infinitely narrow entrance slit and on an optical system that makes use of the entire entrance face of the prism. If the entire entrance face is not used, resolution is decreased accordingly. So an effective length of the prism base b has to be used instead.

### 4.2.3. THE DIFFRACTION GRATING

Diffraction grating is an optical component that is used to disperse a beam of light into its component wavelengths that travel in different directions. They are widely used in spectral analysis, having replaced prisms as optical dispersing elements in most fields[12].

Based on the shape of grooves, diffraction gratings can be divided into two categories: ruled (blazed) and holographic. As shown in the figure below, a ruled (blazed) grating has wedge-shaped groves produced by mechanical ruling, while a holographic grating has a sinusoidal pattern that is produced using holographic recording. Both shapes can be created either on reflective materials (reflective gratings) or transparent materials (transmission gratings). Thanks to the invention of grating precision replication process by White and Frazer in the late 1940's, the diffraction gratings are commercialized and widely used in modern spectrometers[10].
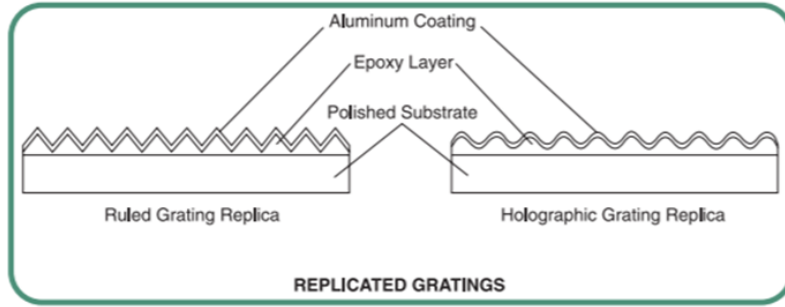


Figure 4.30: Ruled and holographic gratings[10].

#### HOW A DIFFRACTION GRATING WORKS

Before getting into details of the working principle, the well-known grating formula is listed below for easy reference. Whether the diffraction grating is a reflective grating or a transmission grating, there is a general equation:

$$m\lambda = d(\sin\alpha + \sin\beta)$$

Where $\alpha$ and $\beta$ are respectively the incidence angle and diffraction angle of the light. $\lambda$ is the wavelength of the light and $m$ is the diffraction order, which is an integer and $d$ is the groove spacing. Sometimes it is more convenient to use grove density $G$, defined as $1/d$, instead of the groove spacing $d$ because grove density $G$ is the value that can be found written on the side of a grating as lines per millimeter. The grating equation then becomes:

$$Gm\lambda = \sin\alpha + \sin\beta$$

The sign convention commonly used for both transmission grating and reflective grating is that angles measured to the left of the grating normal are positive, while angles to the right are negative.

There is a specific configuration called Littrow configuration, which plays an important role in spectrometers. In Littrow configuration, the incident angle $\alpha$ is equal to the diffraction angle $\beta$, meaning that, taking the reflective diffraction grating for example, light is diffracted back towards the direction of the incident light. Both incident light and diffracted light are thus on the same side of the grating normal. The grating equation then becomes:

$$Gm\lambda = 2\sin\alpha$$

After an overview of the grating formula, the following paragraphs explain how a diffraction grating works and how the grating formula is derived. Diffraction and interference is an illustration or proof of the wave nature of light. The physical phenomena happening in a diffraction grating can be easily understood by always keeping the wave behavior of light in mind.

A monochromatic light source and a zoomed-in view of adjacent two groves (slits) from a reflective diffraction grating are demonstrated and analyzed in the figure below.
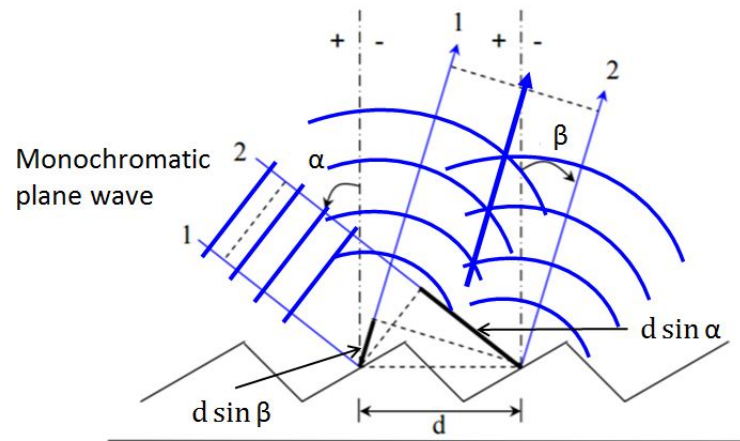
Figure 4.31: Monochromatic beam incident on ruled (blazed) reflective diffraction grating.

When a plane wave of monochromatic light is incident on a ruled (blazed) reflective diffraction grating at an angle $\alpha$ relative to the grating normal, they are reflected on the facets of the grooves and the reflected wave fronts from each grove propagate as spherical waves in all directions just like what is shown in Young's double slit experiment. There exists a discrete set of diffraction angles $\beta$ (direction of propagation) along the spherical wave fronts that, for a given spacing $d$ between two neighboring grooves, the diffracted light from each facet is in phase (In phase means the difference is equal to an integer multiple of the wavelength $m\lambda$) with each other, therefore leading to constructive interference that magnifies the strength of the light waves in the overlapping area. In the same way for the other set of diffraction angles, if the wave fronts are 180° out of phase, destructive interference will be introduced and the light waves are canceled out with each other in the overlapping region.

As shown in the graph above, the light path difference between diffracted light 1 and diffracted light 2 is $d(\sin\alpha + \sin\beta)$. If this value is equal to an integer multiple of the wavelength $m\lambda$, the diffracted light waves 1 and 2 will interfere with each other constructively along the center line of the two diffracted waves, forming a constructive wave twice as the amplitude of each wave.

In this way, in the same diffraction order for a white light source, different wavelengths $\lambda$ have different diffraction angles $\beta$ that have constructive interference, thus leading to the dispersion of incidence light as shown in the figure below. In contrast to the dispersion pattern of prisms, the angular dispersion of gratings increases as the wavelength increases. This explains why the angular dispersion for violet light is less than that for a red light in a grating.
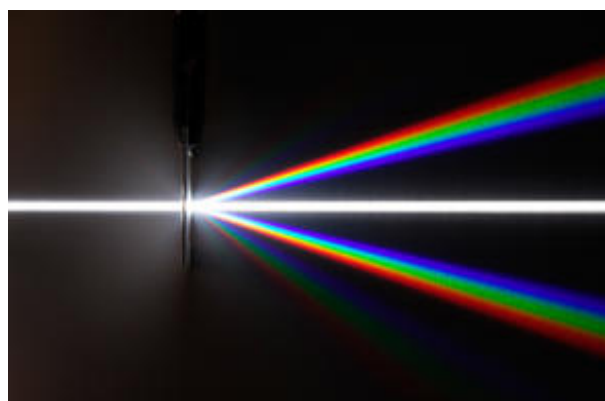


Figure 4.32: White light dispersion by a transmission diffraction grating[11].

### DISPERSION OF A GRATING

The angular dispersion of a grating is defined as $\frac{d\beta}{d\lambda}$. Assuming the incident angle $\alpha$ is constant, which is always the case for a spectrometer setup, the following expression can be derived by differentiation of the grating equation with respect to wavelength $\lambda$:

$$\frac{d\beta}{d\lambda} = \frac{m}{d\cos\beta} = \frac{Gm}{\cos\beta}$$

The linear dispersion is then:

$$\frac{dx}{d\lambda} = \frac{d\beta}{d\lambda}\frac{dx}{d\beta} = \frac{Gm}{\cos\beta}\frac{f_2 d\beta}{d\beta} = \frac{Gmf_2}{\cos\beta}$$

Where $f_2$ is the focal length of the focusing lens.

As can be found in the equation, the angular and linear dispersion increases as the diffraction order $m$ or grating density $G$ increases. An increase in the wavelength of diffracted light waves (larger diffraction angles) also gives rise to the wavelength dispersion. One could also increase the linear dispersion of the incidence light by using a focusing lens of a longer focal length $f_2$.

### RESOLVING POWER OF A GRATING

As mentioned in the prism section, the resolving power of a grating $R = \frac{\lambda}{d\lambda}$ also defines its ability to separate two neighboring lines near wavelength $\lambda$ with a separation of $d\lambda$ and it makes use of Rayleigh criterion for resolution again.

For a diffraction grating, the theoretical resolving power is defined, assuming infinitely narrow entrance slit:

$$R_{theoretical} = |m|N$$

Where $m$ is the diffraction order and $N$ is the number of grooves that is illuminated. The proof this formula can be found in a textbook written by William G. Schrenk[7] and a lecture handout, written by B.E.Sauer[39].

As can be found in the equation that the theoretical resolving power reaches its maximum, just like the situation for a prism, when the entire face of the grating is illuminated by the incidence light beam.

However in practice no entrance slit is infinitely small, so in this way another practical resolving power equation is derived using conservation of Etendue, found in an article [40].

$$R_{real} = \frac{|m|Nf_1\lambda}{s}$$

Where $s$ is the width of the entrance slit and $f_1$ is the focal length of the collimating lens. As can be seen in this equation, one could increase the resolving power by reducing the width of an entrance slit or increasing the focal length of a collimating lens.

### Anamorphic magnification of a diffraction grating

Anamorphic magnification for a diffraction grating means that the magnification factor along the plane of dispersion is larger than that of the other plane perpendicular to the plane of dispersion. Taking a look at the figure of the grating equation, the width of the incidence light beam $D_1 = d \cos \alpha$ while the width of the diffracted beam $D_2 = d \cos \beta$. In this way, the diffracted beam along the plane of dispersion is magnified in a factor of

$$\frac{D_2}{D_1} = \frac{\cos \beta}{\cos \alpha}$$

However the width of the beam along the plane perpendicular to the plane of dispersion remains the same. The anamorphic magnification will be removed if Littrow configuration ($\alpha = \beta$) is implemented.
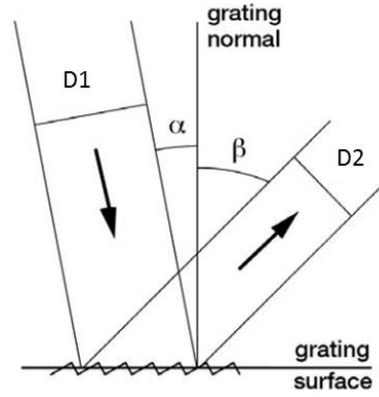


Figure 4.33: Anamorphic magnification of the incidence beam[12].

Due to this effect, a "stretching factor" is added to the size of a spectral image along the plane of dispersion while the direction perpendicular to the plane of dispersion is not influenced. Using the conservation of Etendue, the magnification factor along the plane of dispersion (slit width) can be computed[40][41]:

$$\frac{W_2}{W_1} = \frac{\cos \alpha}{\cos \beta} \frac{f_2}{f_1}$$

While the other direction (slit height) is not affected by this phenomenon:

$$\frac{H_2}{H_1} = \frac{f_2}{f_1}$$

The significance of this relation is that one could simply eliminate the image distortion resulting from diffraction grating by putting it into Littrow configuration.

## 4.3. SPECTRAL IMAGING TECHNOLOGIES: SCANNING AND SNAPSHOT DEVICES

Spectral imaging, also known as hyperspectral imaging, multispectral imaging, aims to collect spectral information of light that is emitted, reflected, or transmitted from different materials, defining the material based on its unique spectral signature. The spectral information $I(x, y, \lambda)$ is often visualized as a so called "datacube" with two dimensions in space and one dimension in wavelength. However for time-resolved systems, the spectral information $I(x, y, \lambda, t)$ is called "hypercube" with an additional dimension in time. They are stored in pixels, which can be treated as an element in detector arrays or a spatial location in a datacube or hypercube.

The spectral information can be either collected in a time-sequential manner by scanning one column (whiskbroom spectrometer), one line (pushbroom spectrometer) or one wavelength (filtered camera) at a time or by simply capturing the whole scene in a single detector integration period, as demonstrated in figure below. These two technologies are called scanning and snapshot separately. A snapshot spectrometer is also equal to the slitless spectrometer used in this thesis.



Figure 4.34: The part of datacube collected for (a) scanning, and (b) snapshot devices during a single detector integration period [13].

There are basically three categories of scanning spectrometers: point-scanning, line-scanning and wavelength-scanning spec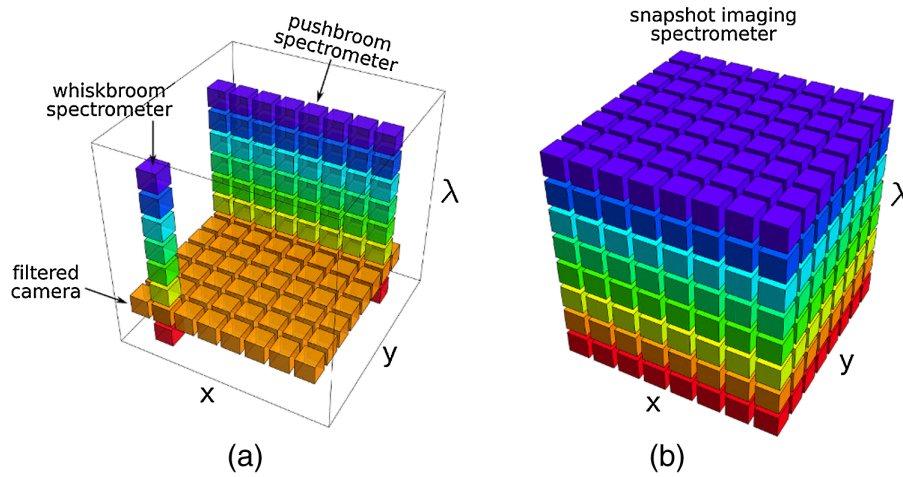trometers. A whiskbroom spectrometer is a point-scanning spectrometer, which utilizes a linear array of detectors to scan across the two spatial dimensions of the datacube, collecting a column of information at a time. A pushbroom spectrometer is a line-scanning spectrometer that uses a 2D detector array to scan across the y direction, collecting a vertical slice of the datacube at a time. A filtered camera is constituted by installing a filter wheel or tunable spectral filter in front of a camera, and it collects a horizontal slice of the datacube at one integration period, thus requesting scanning along the spectral dimension to accomplish the datacube collection[13].

Compared with scanning instruments, the main advantage for snapshot is high light collection (optical throughput), which can be remarkable especially for large datacubes[13]. Besides, snapshot instruments also lack scanning artifacts because of the lack of moving parts.

Although snapshot devices generally provide much higher light collection efficiency than comparable scanning devices, the snapshot system does not by itself mean high light throughput if the system architecture contains spatial and/or spectral filters[13]. In addition, snapshot devices are not necessarily faster than scanning devices. Snapshot devices can also have very long measurement time. The essential difference between those devices is that snapshot devices collect the whole datacube by a single detector integration period, and whether the collecting time is long or short hinges on the application[42].

Nowadays, the division between snapshot devices and scanning devices are not that distinct. Designers have mixed both architectures so that, for scanning devices, the scanning measurement time is significantly decreased and the light throughput is increased by even a factor of 4[42].

# 5

# EXPERIMENTAL SETUP

In this chapter, the components and devices used in the experiment will be firstly explained, followed by the description of the layout of the two experimental setups.

## 5.1. AN OVERVIEW OF THE EXPERIMENTAL EQUIPMENT

### 5.1.1. THE LIGHT SOURCE AND THE BURNER

The experiment basically consists of two parts, one of which uses the helium–neon laser or simply HeNe laser as a light source while the other uses the Bunsen flame as a light source.

The wavelength of the HeNe laser locates in the red part of the visible spectrum, which is $692\,nm$ according to given information of the product. It is able to generate a highly collimated light beam of a high intensity.

The Bunsen flame uses the pure methane as fuel and air as the oxidizer and it is produced by the Bunsen burner originally designed for students to measure laminar burning velocity in a course, as shown in the diagram below.
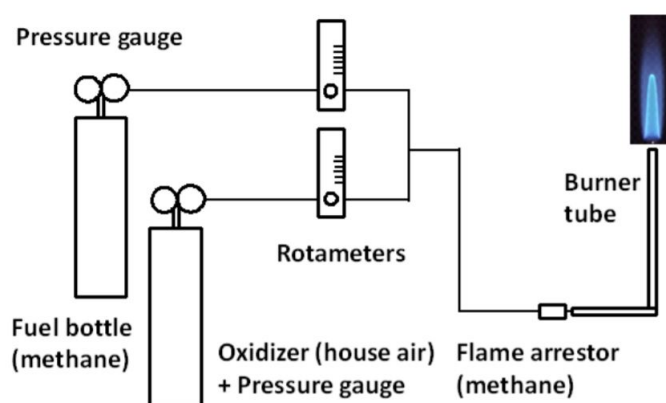


Figure 5.1: A schematic diagram of the Bunsen burner taken from the exercise sheet[14].

The Bunsen flame is a pre-mixed flame and the individual volumetic flow rate ($L/min$) of the air and methane can be controlled independently by adjusting the two rotameters. The maximum attainable flow rate for the air flow is 10 $L/min$ while that of the methane flow is 1 $L/min$. The fuel/air mixture is then fed through a long stainless steel pipe that has a diameter to length ratio of 1 : 100, which should be more than sufficient for the development of a laminar flow and thus laminar flame.

The setup is very safe to operate since it is designed in a way that the flow velocity of the fuel/air mixture is way larger than the possible burning velocity so that the flash-back of the flame is prevented to the maximum extent. In addition, the flame arrestor in the right corner of the diagram is also used to quench the back propagation of the flame.

### 5.1.2. THE POINT-SPECTROMETER

The point-spectrometer used to obtain the wavelength information of a light source is a fiber-based Czerny-Turner CCD spectrometer: Thorlabs CCS100[15]. The detection range of wavelength, according to their website, is between $350nm$ and $700nm$, which should be sufficient to capture the peaks of CH and $C_2$ in the visible range. The absolute efficiency of the grating, defined as the ratio between the power of diffracted light to the power of incidence light on the grating, is also designed to peak at the blaze wavelength $500nm$ in this spectrometer. In this case, the spectrum of interest from $400nm$ to $600nm$ which contains the band heads of both species can be captured to a great extent. The absolute grating efficiency diagram of CCS100 spectrometer is shown below.
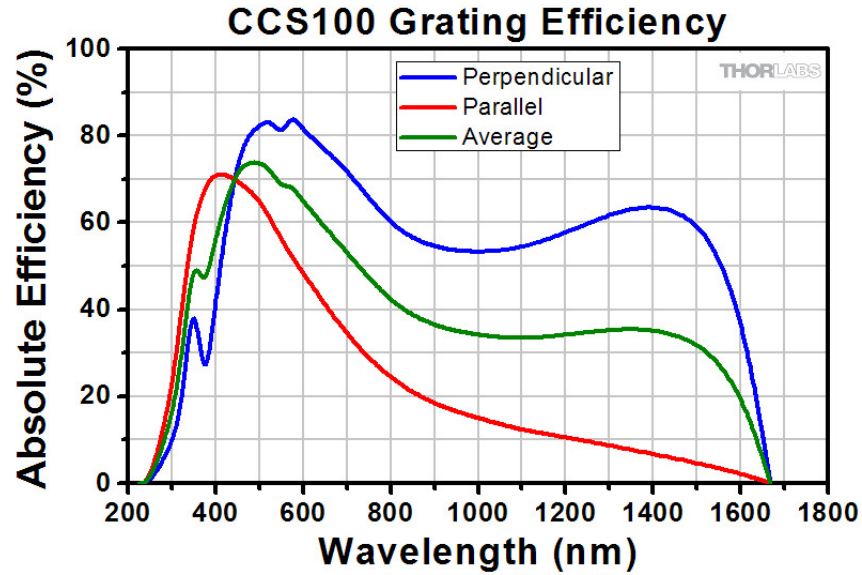


Figure 5.2: CCS100 absolute grating efficiency[15]. 3 colors indicate 3 polarization directions with respect to the lines of the grating.

A general arrangement of a Czerny-Turner CCD spectrometer is shown in the diagram below. The efficiency or sensitivity of the components inside the spectrometer are all wavelength dependent, including the mirrors, the grating, and the sensor. Therefore Thorlabs CCS100 spectrometers are amplitude corrected before shipment, according to their website[15].
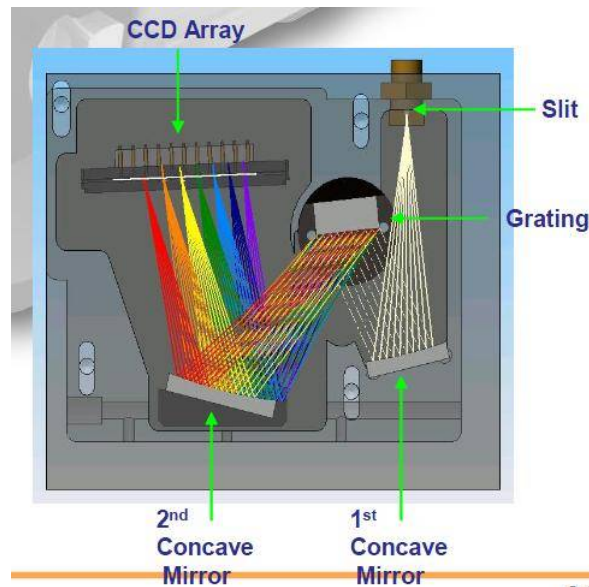


Figure 5.3: A general arrangement of Czerny-Turner CCD spectrometers[16].

### 5.1.3. THE LENSES

The lenses used in this project can be divided into 2 categories: single lens and compound lens.

#### THE SINGLE LENSES

All of the single lenses are N-BK7 plano-convex lenses with anti-reflective coating: 350 - 700 $nm$, produced by Thorlabs[17]. During this project, 3 focal lengths: $100mm$, $200mm$, and $300mm$ are used and the diameter of all single lenses is identical, which is $50.8mm$. The transmission rate for an uncoated sample is shown below:
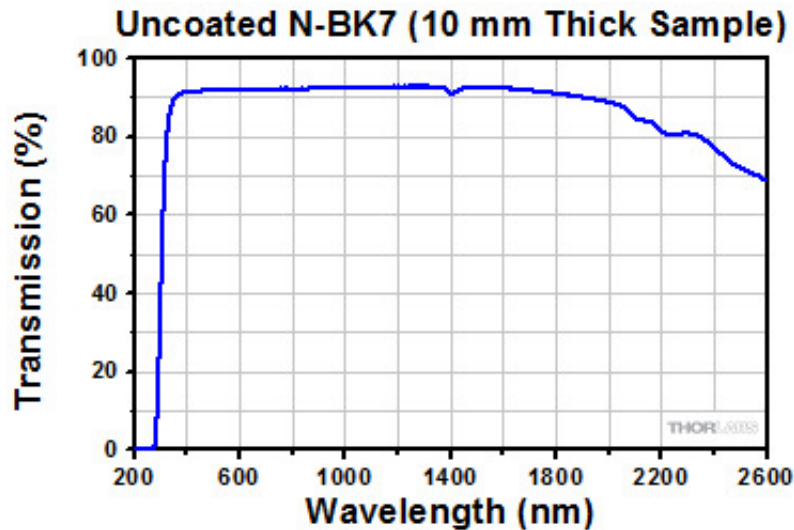


Figure 5.4: Transmission efficiency for an uncoated N-BK7 plano-convex lens sample [17].

As can be found in the graph, the transmission rate for wavelengths between $400nm$ and $600nm$, the spectrum range of interest, is around 90%, which does not have much difference. With the AR coating applied, according to the manufacture's website, the transmission rate could even reach 99.5% per surface in average across the designed spectral range for an incidence angle between 0° and 30°[17].

#### THE COMPOUND LENSES

There are two types of compound lenses available in this project: Nikon AF Nikkor 35mm f/2D and Nikon AF Nikkor 50mm f/1.8D. Both of the lenses are prime photography lenses that have fixed focal lengths of $35mm$ and $50mm$ respectively and both types are composed of 6 lens elements. The overall transmission efficiency for both lenses is around 90%, as tested by DxOMark[43]. The spectral transmission efficiency data cannot be found, which should however not have a big difference in the visible range since they are designed for photography.

The reason to use the compound lenses is that firstly they are designed to reduce lens aberrations so that they can provide a better image quality; secondly they have relatively shorter focal lengths, which are beneficial for a larger field of view, allowing more spectral images to be captured at the same time.

### 5.1.4. THE GRATING

The diffraction grating used in this project is a 1200 $Grooves/mm$ and 50 $mm \times$ 50 $mm$ visible transmission grating produced by Thorlabs[18]. The absolute grating efficiency test data can be found in their website, as shown below. However the exact testing condition for this data such as incidence angle is unknown and the efficiency curves do vary with incidence angles, so this graph can only give readers a general reference.
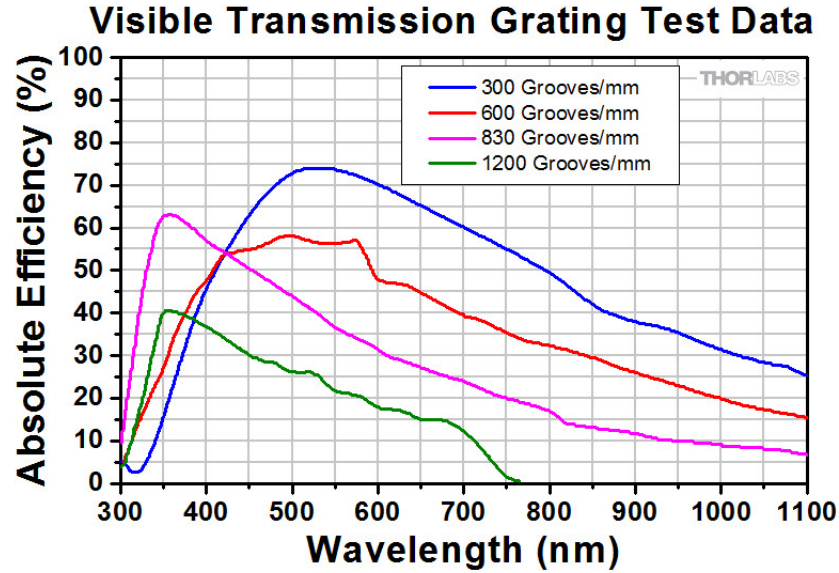


Figure 5.5: Absolute grating efficiency curves for Thorlab visible transmission gratings [18].

### 5.1.5. THE CAMERA HEAD

The camera head is composed of three parts: the imaging sensor, the 35$mm$ camera lens mentioned above, and finally a 300$mm$ plano-convex lens. The imaging sensor is connected to the camera lens via a C-mount. Ideally, the distance between the camera lens and the imaging sensor should be enough to allow an image formed exactly on the sensor plane. However currently no spacer of proper size can be found to install between the sensor and the camera lens, consequently resulting in that images are always formed behind the imaging sensor plane even with the maximum focusing ring setting. Therefore in order to solve this problem an additional 300$mm$ plano-convex lens has to be assembled in front of the camera lens in order to help form the image on the sensor plane. The distance between the imaging sensor and the camera lens can be adjusted by turning the focusing ring on the camera lens. A photo of the combined camera head is shown below.

Figure 5.6: The combined camera head which is composed of 3 elements. From left to right: $300mm$ plano-convex lens, the camera lens, and the imaging sensor.

The imaging sensor used in the thesis project is a WinCamD-LCM beam profiling camera[19]. It makes use of a CMOS detector that is able to work in the wavelength range between $355nm$ and $1150nm$. It has a full resolution of 2048 × 2048, which is about 4.2 Mega pixels. The dimension of each pixel is 5.5 × 5.5 $\mu m$. During the capturing process, two modes can be selected: full mode and fast mode. Fast mode makes use of every two pixels so that, in comparison to full mode, the pixel dimensions turns to be 11.0 × 11.0 $\mu m$, which are twice as large.

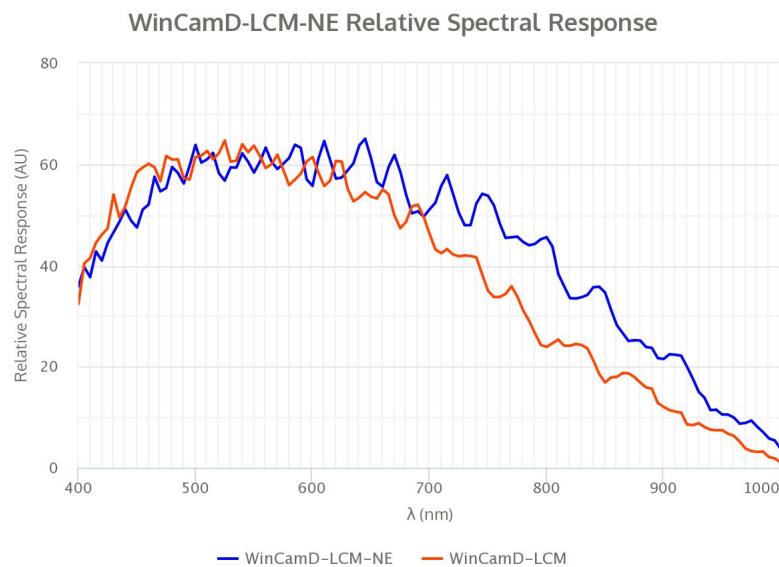The spectral response of the imaging sensor, found in the manufacture's website, is shown in the graph below.



Figure 5.7: WinCamD-LCM beam profiling camera spectral response[19].

### 5.1.6. The calibration targets

For calibrating the skewing of the images, two calibration targets are designed in this project with one being a checkerboard pattern and the other being a right triangle, as shown in the photo below. Since the black painting cannot satisfactorily block the incidence light, the author at the end applies some blue painting around the target, as can be seen in the left photo.
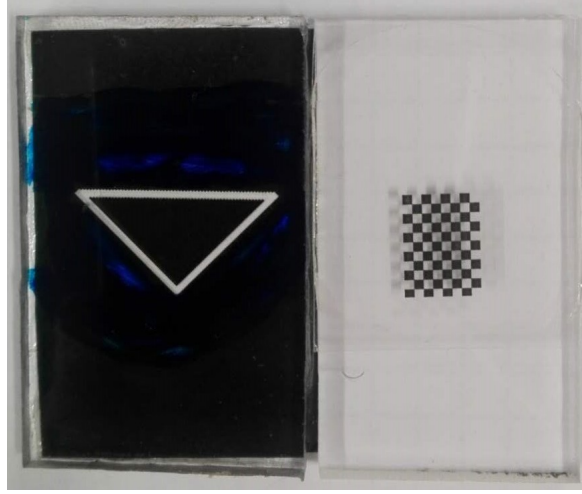


Figure 5.8: The two calibration targets: right triangle on the left and checkerboard pattern on the right.

At best, the checkerboard pattern should be made large enough to completely fill in the field of view of a camera so that the distortion at every corner of the image can be recorded. Nevertheless due to the limited size of the laser beam, in order to achieve an even illumination (otherwise the edge of the pattern is hard to be recognized by the software) on the target, only the central part of the beam can be used and the target has to be made relatively small, which has a dimension of $4 \times 5$ black squares with each square being $1 \times 1 \ mm$.

For finding out the possible distortion in an image of the real flame and also for a more even illumination, the right triangle pattern is made to be comparable to the size of the Bunsen flame. The length of the right-angle side is about $15mm$ and the width of each edge is $1mm$.

Both of the targets are printed on transparency paper and then glued on two separate pieces of transparency plastic.

## 5.2. Design of a monochromatic synthetic flame using HeNe laser

For investigating the wavelength dependent features in an imaging system, a monochromatic laser source, $692mm$ HeNe laser has been employed. The synthetic flame design is made up of two elements: an illumination system and an object target. The object target can be any pattern as long as the illuminating light can pass through it. Both a schematic diagram and a photo of the illumination system is shown below.
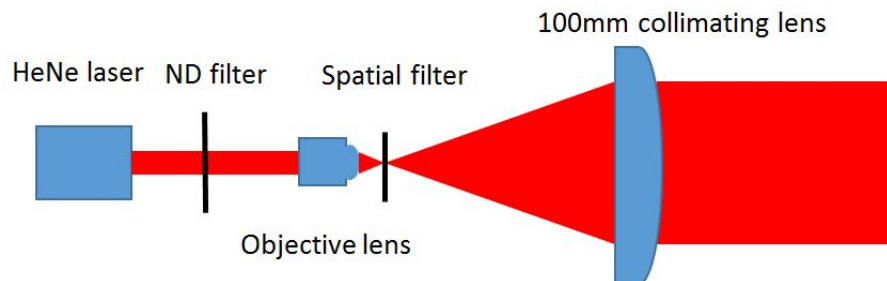


Figure 5.9: A schematic diagram of the illumination system.
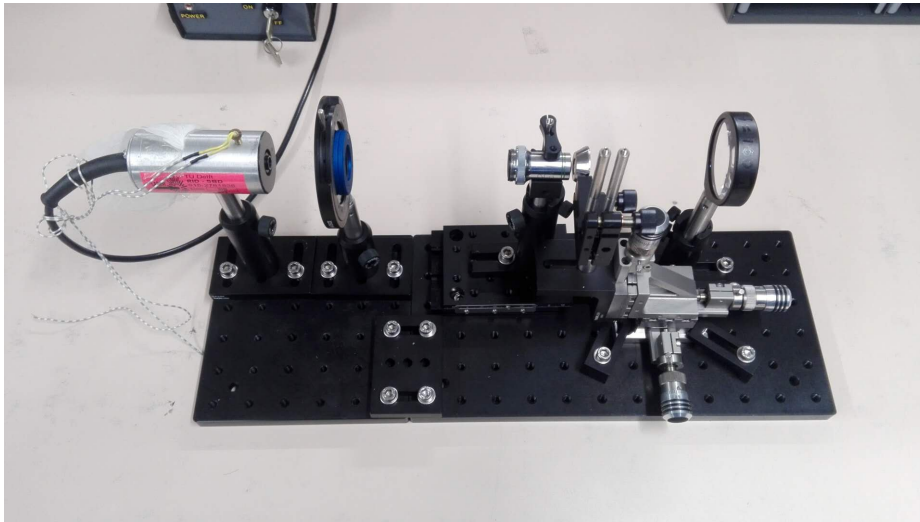
Figure 5.10: A photo of the illumination system.

As can be seen in this diagram, the combination of the objective lens and the collimating lens is used to expand the laser beam. ND filter is a filter used to decrease the intensity of the laser beam and the spatial filter, in this case a pinhole, is used to increase the quality of the spatial profile of the laser beam by blocking the high spatial diffraction order caused by the objective lens, which is however optional for this setup. The pinhole in the end is removed from this setup because it is too sensitive to external disturbance that even a touch of the table has an influence on its behavior, making the mainstream of the light beam blocked by the pinhole.

The collimated laser beam is then used to illuminate the object target, which is the checkerboard pattern and the 1951 USAF resolution test target made by Thorlabs in this project. The illuminated object can then be treated as a monochromatic synthetic flame source that is specifically designed to study wavelength dependent skewing of the image.

Since the checkerboard target is pretty small, for achieving a proper size of image on the imaging sensor, a de-magnification factor of 0.25 is set. The imaging system used for this setup is thus made up of: a collimating lens ($200mm$ plano-convex lens), a transmission grating that disperses horizontally, the $50mm$ camera lens, and finally the imaging sensor.

## 5.3. DESIGN OF A SLITLESS SPECTROMETER

The slitless spectrometer is basically composed of 3 parts: a collimating lens ($300mm$ plano-convex lens), a transmission grating, and the camera head. Two configurations are allowed for this setup with the first configuration called horizontal dispersion configuration and the second vertical dispersion configuration. The apparatus is shown in the pictures below.

As can be seen in the pictures, the incidence angle of light beams on the grating surface is equal to the grating deflection angle, which is adjustable along the horizontal axis (vertical dispersion configuration) and the vertical axis (horizontal dispersion configuration). The object such as calibration targets and Bunsen flame are placed at one focal length $300mm$ away from the collimating lens.
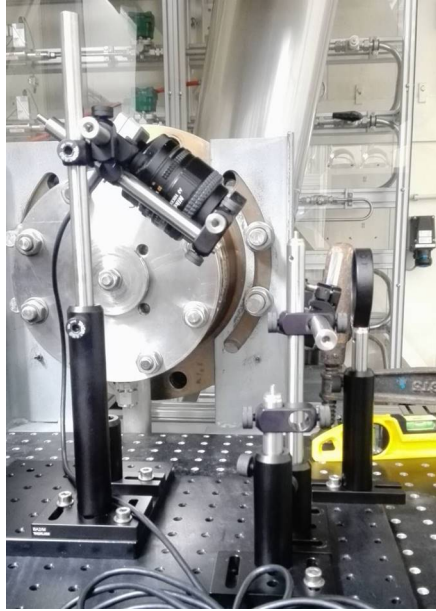


(a) Vertical dispersion configuration side view
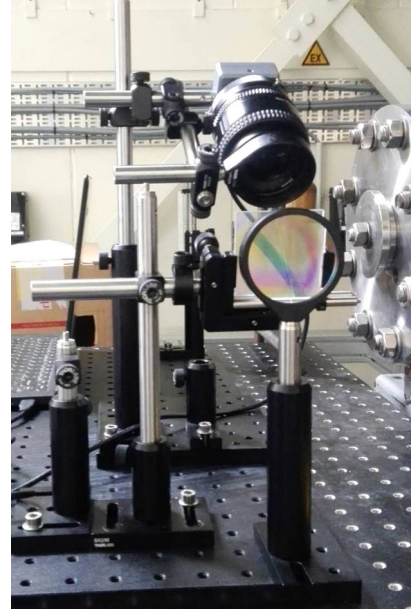
(b) Vertical dispersion configuration front view

Figure 5.11: The slitless spectrometer in vertical dispersion configuration. From right to left: a $300mm$ plano-convex lens, a transmission grating, and the camera head.



(a) Horizontal dispersion configuration side view

(b) Horizontal dispersion configuration front view

Figure 5.12: The slitless spectrometer in horizontal dispersion configuration. From right to left: a $300mm$ plano-convex lens, a transmission grating, and the camera head.

# 6

# RESULTS AND ANALYSIS

In this chapter, the spectrum data obtained by the point spectrometer and the proposed two setups in last chapter will be discussed.

## 6.1. THE SPECTRUM OF A BUNSEN FLAME

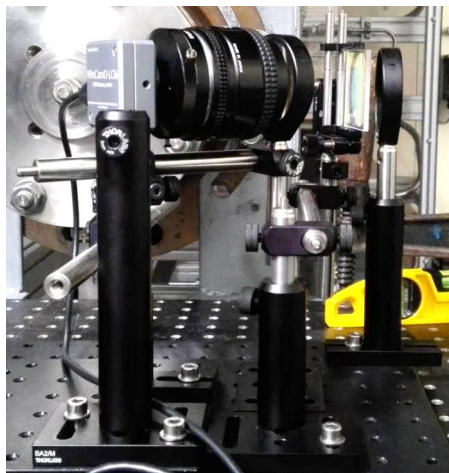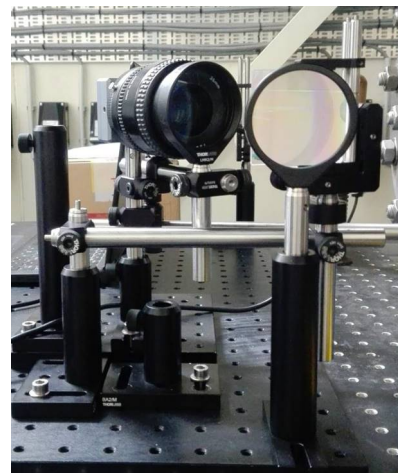The Bunsen flame tested in this project gives in general a blue-greenish color. However it changes from violetish to greenish as the burning condition changes from fuel lean to fuel rich. The change in color basically results from the change in relative concentration of CH and $C_2$ species. The strongest band head of CH locates at the wavelength around $431nm$, giving a violet color while the strongest band head of the $C_2$ radical locates at $514nm$, which is in the range of green color. As the equivalence ratio increases, the ratio of $C_2$ over CH increases, so the flame looks more greenish.

In order to guarantee the concentration of CH and $C_2$ in the Bunsen flame is in a good balance that both of them have a strong signal, the equivalence ratio is set 1.2 based on rule of thumb. Since the main focus of this thesis project is imaging of the Bunsen flame, the relation between equivalence ratio and the relative content of these species is left for future research.

The spectrum is taken from the left bottom point of the reaction zone, as demonstrated in the figure below. It has also been validated with the results from Zizak's research[26]. The reason of choosing this point is that the flame is more stable (less fluctuation) in the bottom than in the top so the measuring point in the reaction zone should always be the same.
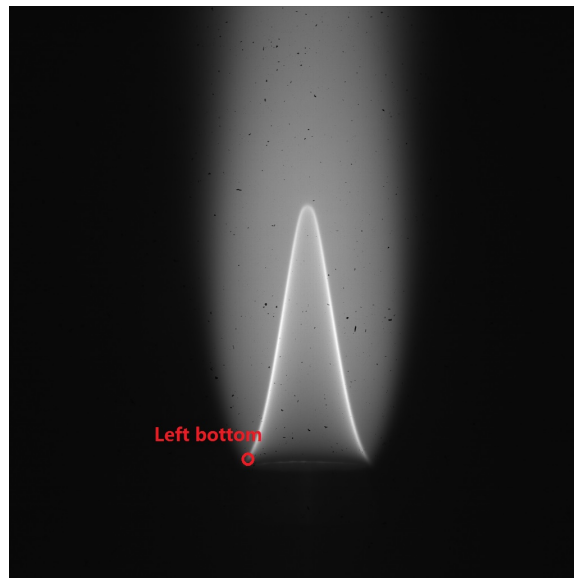


Figure 6.1: The location at which the spectrum is take from.
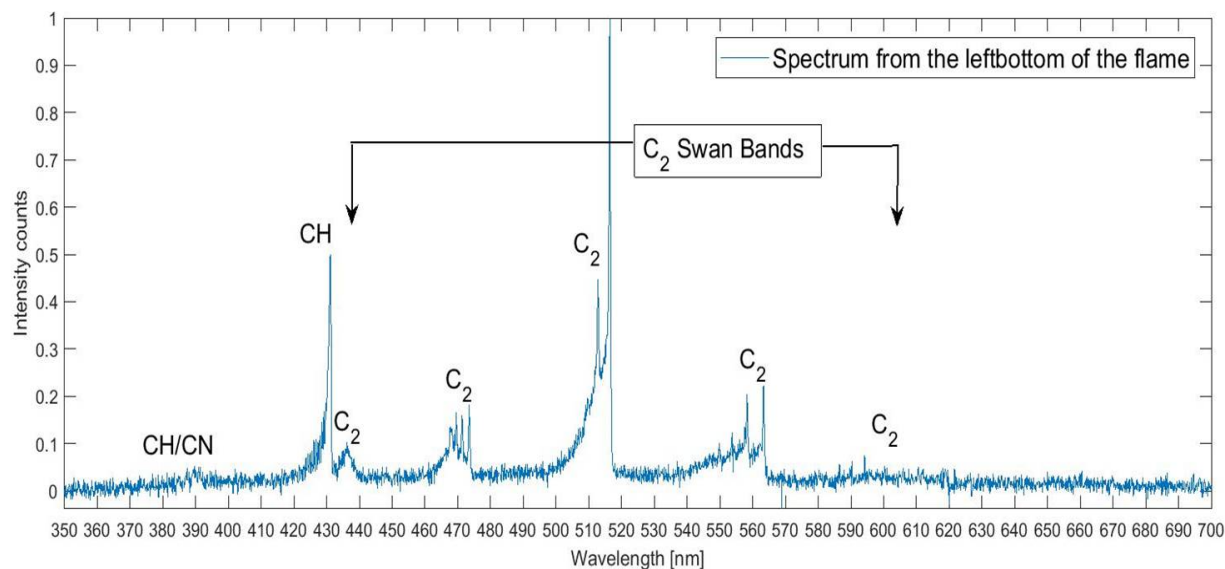
Figure 6.2: The normalized spectrum of the Bunsen flame with an equivalence ratio being 1.2, taken from the left bottom of the conical shape.

The spectrum is captured by forming an image on the probe of the point-spectrometer using the $100mm$ lens that positions at $2f$ away from the flame. In order to increase the signal to noise ratio, an average of 10 times of capturing is made with an integration time of $9000ms$ each (more averages does not produce better results). The author finds the combination of longer integration time and a lower intensity image can produce the best signal to noise ratio.

As discussed before, the point-spectrometer is already calibrated for both wavelength and amplitude and the imaging lens has almost identical transmission rate in this spectral region. Therefore the height of these peaks can give readers a valuable insight into the relative percentage contents of each radical. The relative content of CH and $C_2$ species in the reaction zone can be analyzed by comparing the intensity of each peak.

## 6.2. THE RESULTS OF THE MONOCHROMATIC SYNTHETIC FLAME DESIGN

The objective of designing such a monochromatic synthetic flame with strong intensity is to study the wavelength dependent skewing of the image. Since the incoming light is monochromatic, after grating dispersion only one single wavelength in the first order of diffraction is achieved. In this way, there is no need to consider spectral overlapping and therefore the skewing caused by a diffraction grating which is dependent on wavelength can be easily verified.

In this section, the exact wavelength of this HeNe laser will be measured first for verifying whether it has a narrow band spectrum. Secondly, 3 incidence angles will be chosen to study anamorphic magnification of a diffraction grating and a comparison will be made between calculation values and experimental values. Finally, a calibration of the distorted image will be conducted using a Matlab built-in tool called single camera calibration .

### 6.2.1. THE SPECTRUM OF THE HENE LASER

The spectrum of the HeNe laser is shown in the diagram below. As can be found in the diagram, the spectrum is comparatively narrow and it peaks around 692.8 $nm$, which is a little different from what is written on the laser tube. However due to its narrow spectrum, it is acceptable to treat the HeNe laser as a monochromatic light source.
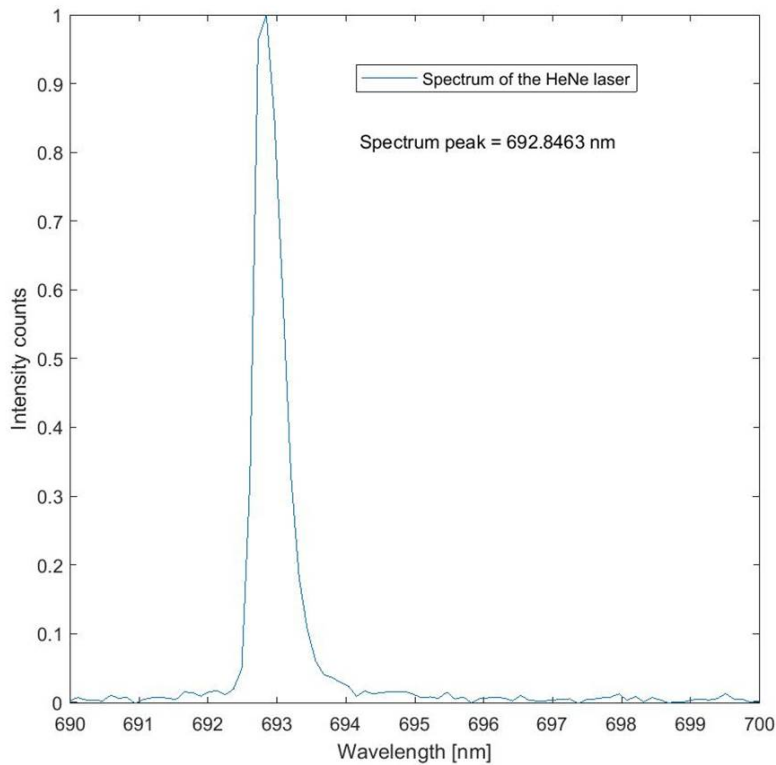


Figure 6.3: The normalized spectrum of the HeNe laser.

### 6.2.2. 0° INCIDENCE ANGLE

Instinctively, without any knowledge of image skewing caused by a diffraction grating, one would firstly set the deflection angle of a diffraction grating to be 0°, which is perpendicular to incoming light rays. The image of the checkerboard target then appears to be significantly skewed, as shown below.



Figure 6.4: Image of the checkerboard calibration target at 0° incidence angle (1st order). Bending of the edges is a result of lens pincushion distortion magnified by grating's anamorphic magnification.

The dimension for each black square is $1 \times 1$ $mm$, but the image of it is skewed along the plane of dispersion. The aspect ratio for each black square image becomes 1.81 in average.

According to the grating formula, the diffraction angle for this HeNe laser is calculated to be 56.3°. The aspect ratio based on grating anamorphic magnification formula is thus:

$$\frac{\cos \alpha}{\cos \beta} = \frac{\cos 1°}{\cos 56.3°} = 1.8$$

It is interesting to find that this theoretical anamorphic magnification factor is highly consistent with the experimental value.

### 6.2.3. LITTROW ANGLE CONFIGURATION

In order to eliminate anamorphic magnification caused by a diffraction grating, Littrow configuration needs to be implemented. Based on the grating formula, the Littrow angle is calculated to be 24.6°. However the current measuring tool cannot reach the accuracy of one decimal place, the deflection angle is thus set to be 25°. The result is shown in the figure below.



Figure 6.5: Image of the checkerboard calibration target at 25° incidence angle (1st order). Bending of the edges is a result of lens pincushion distortion magnified by grating's anamorphic magnification.

As can be seen in the result above, the image skewing has been removed obviously. The average aspect ratio is measured to be 1.01, which is extremely close to the calculated value 0.99. So one could say that the

result under Littrow condition is free of anamorphic magnification. In addition, resulting from the decrease in anamorphic magnification, there is obviously less bending of the edges in comparison to the previous image.

### 6.2.4. 18° INCIDENCE ANGLE

For the reason of having some visible skewing for the following image calibration, the deflection angle of the diffraction grating is set to be 18° in this test, which is not only close to the Littrow angle but also produces a bit but not too much skewing of the image.
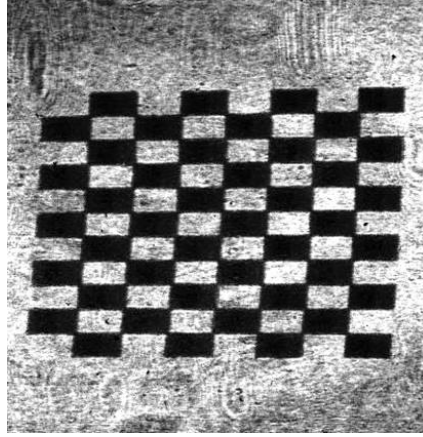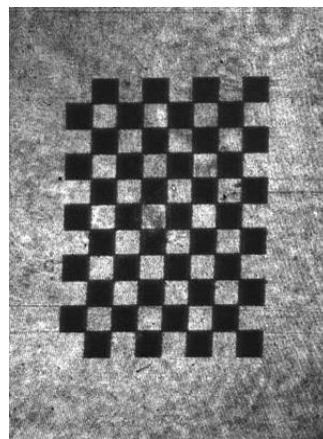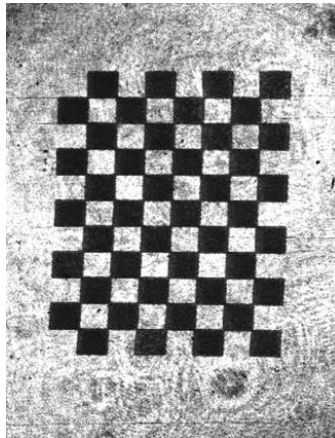


Figure 6.6: Image of the checkerboard calibration target at 18° incidence angle (1st order). Bending of the edges is a result of lens pincushion distortion magnified by grating's anamorphic magnification.

As can be seen in the image above, when the incidence angle is set close to Littrow angle, the amount of image skewing is reduced greatly and the aspect ratio now becomes 1.11, which is very close to the aspect ratio calculated using grating anamorphic magnification formula: 1.12.

### 6.2.5. IMAGE DISTORTION CALIBRATION

When taking an image of an object, in order to maintain the real shape of an object, lens distortions have to be as minimum as possible. In particular for imaging spectroscopy, anamorphic magnification of a diffraction grating always aggravates the skewing of an image, magnifying the amount of distortion along the plane of distortion. In addition to include more sophisticated optical system for minimizing lens distortion, it is also necessary to investigate how to correct a lens distortion using image post-processing method.

A built-in tool in Matlab called single camera calibration is used to correct the distortion in the 18° incidence angle image. During the calibration process, intrinsics, extrinsics, and lens distortion parameters are firstly estimated by analyzing the image of a checkerboard pattern of known dimensions, followed by using these parameters to undistort images of the target object placed at the initial position where the checkerboard pattern is. The description of this tool is listed here for readers' interest[44].

The result of 18° incidence angle is used as the calibration target. The images before and after calibration of both checkerboard pattern and the object (USAF 1951 resolution test target) are presented below.
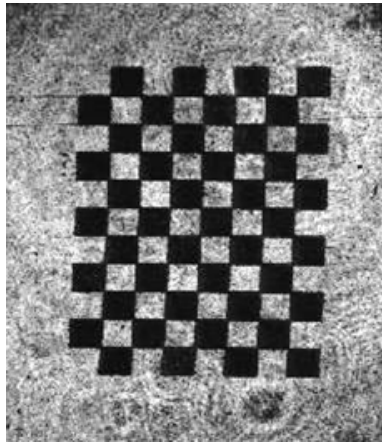
(a) Checkerboard before calibration
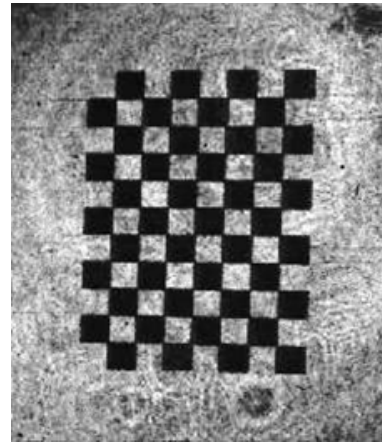


(b) Checkerboard after calibration

Figure 6.7: The calibration of a checkerboard pattern. Compared to the original aspect ratio for each square 1.11, the calibrated aspect ratio turns to be 1.01 on the right photo.
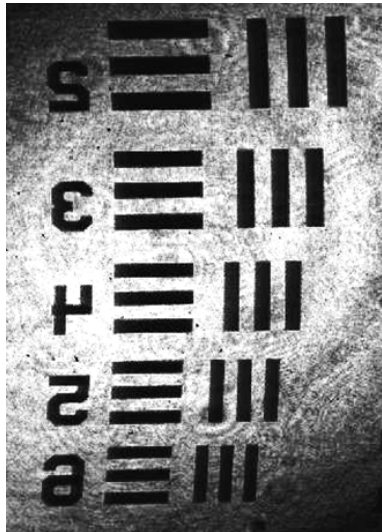


(a) Object before calibration
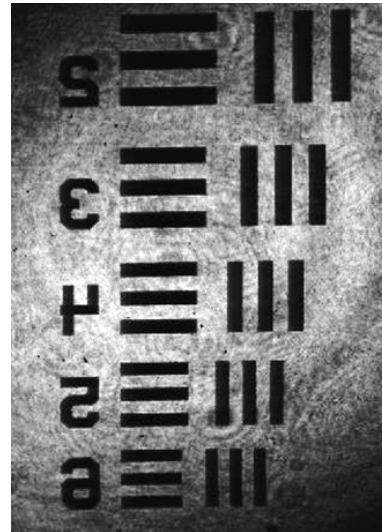


(b) Object after calibration

Figure 6.8: The calibration of the object (USAF 1951 resolution test target).

As can be found in these images, the horizontal stretching or skewing along the plane of dispersion has been largely recovered and the bending of the edges, as a result of magnified pincushion distortion, has also been removed significantly.

## 6.3. THE RESULTS OF SLITLESS SPECTROMETER DESIGN

The objective of this setup is to achieve simultaneous capturing of CH and $C_2$ images in the visible range. In order to analyze the spatial distribution of these species, the wavelength-dependent image skewing should be minimized, thus requiring the diffraction grating to be at Littrow configuration.

In this section, the results of the 2 configurations of this slitless spectrometer design will be discussed. Firstly, The corresponding radicals of spectral images will be identified by comparing them with the spectrum graph collected by the point spectrometer. Then the wavelength-dependent skewing of an image will be studied and in the end a calibration method used for this slitless spectrometer design will be proposed.

### 6.3.1. HORIZONTAL DISPERSION CONFIGURATION

According to the grating formula, Littrow angle for the maximum peak of CH ($431nm$) is $15°$. So the deflection angle of this transmission grating is set to be $15°$. The figure below shows the stitched photo of 0th order flame image and the 1st order dispersion of the conical Bunsen flame captured by horizontal dispersion configuration.



Figure 6.9: Results of the horizontal dispersion configuration in the $15°$ Littrow configuration setting. The direction of dispersion is towards the right of the paper.

The 1st order spectral image is then compared to the spectrum data. As can be seen in the figure below, generally 4 groups of bands can be discerned in this configuration. One of the advantages of horizontal dispersion is that, taking a closer look at each group, the transition details within the same group is also well dispersed, which can be identified by counting the spectral peaks. The number of spectral peaks is highly consistent with the spectrum data captured by the point-spectrometer, as shown in the figure below.



Figure 6.10: Spectral images identification with the spectrum data. From left to right, the radicals can be identified as CH ($431nm$), $C_2$ ($436nm$), $C_2$ ($473nm$ 4 peaks), $C_2$ ($514nm$ 2 peaks), and $C_2$ ($563nm$ 4 peaks).

Even though the horizontal dispersion is beneficial for discerning spectral details within the same band

group, another band group of CH/CN that locates around $390nm$ is however barely captured (only extremely faint silhouette). This is probably because the horizontal dispersion configuration is not very sensitive to a spectral image of considerably low intensity, or in another word, it tends to blur very faint spectral images with a relatively broader band more.

### 6.3.2. VERTICAL DISPERSION CONFIGURATION

Just as the horizontal dispersion configuration, the deflection angle is set to be $15°$, which is the Littrow angle of CH ($431nm$). The only difference for the setting of diffraction grating is that now the incidence light rays are diffracted upwards. The figure below illustrates 0th order and 1st order spectral images that are stitched together afterwards. The image has been rotated $90°$ clockwise for the reason of layout.
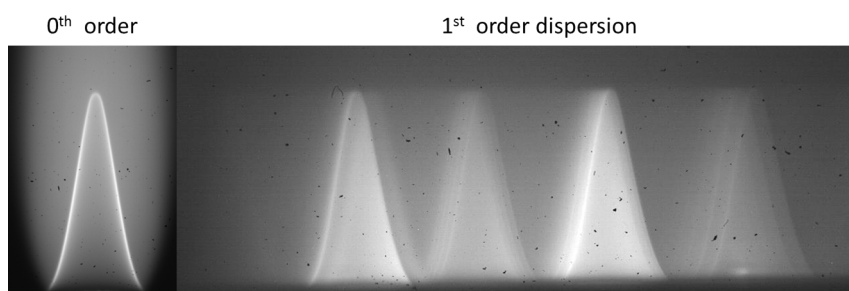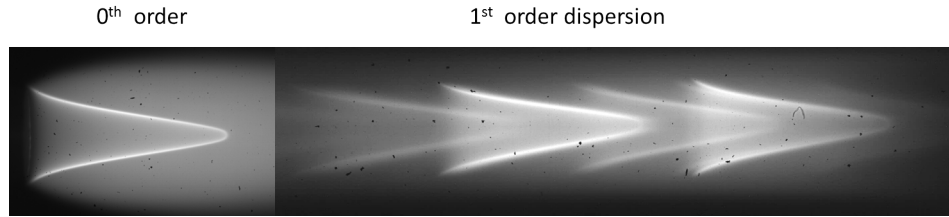


Figure 6.11: Results of the vertical dispersion configuration in the $15°$ Littrow configuration setting. The direction of dispersion is towards the right of the paper.

The result is then compared to the spectrum data. It is apparent that 5 groups of bands can be captured in this configuration. The fifth band from left in this case is merely captured because the light from this band incidents on the edge of the camera lens so that only a small portion of light can be collected. Compared with the horizontal dispersion configuration, 1 more band group is recorded, which is CH/CN that locates around $390nm$. However the transition details within the same band group cannot be discerned in this configuration. There is only a slight separation between two adjacent $C_2$ peaks at the bottom of the $C_2$ ($514nm$) band group. It is interesting to find that since the transition details are overlapped with each other within the same group, each band group of this configuration also has a relatively higher intensity and thus a clearer boundary.
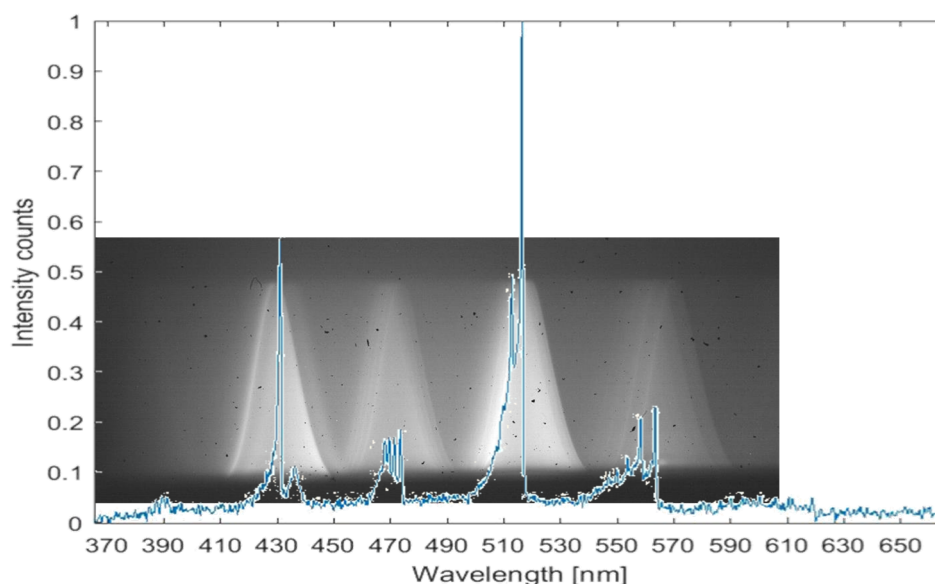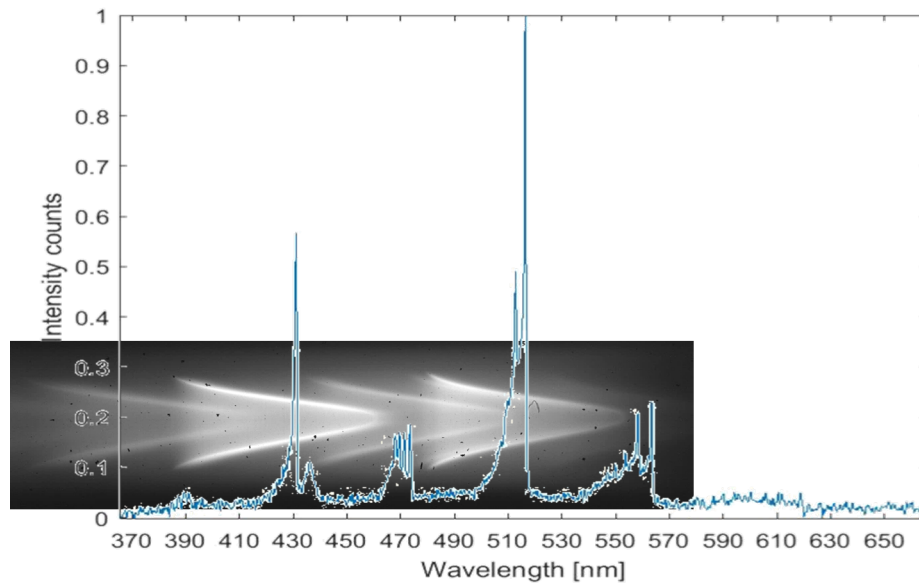


Figure 6.12: Spectral images identification with the spectrum data. From left to right, the radicals can be identified as CH/CN ($390nm$), CH ($431nm$), $C_2$ ($436nm$), $C_2$ ($473nm$), $C_2$ ($514nm$), and $C_2$ ($563nm$).

The intensity diagram of each band group obtained from the left bottom point indicated in figure 6.1 is plotted on top of the spectrum of the point-spectrometer, as shown below. Although the spectral responsivity is wavelength-dependent and thus requires further calibration, the figure below can give readers a general

idea of the intensity distribution in the current result.
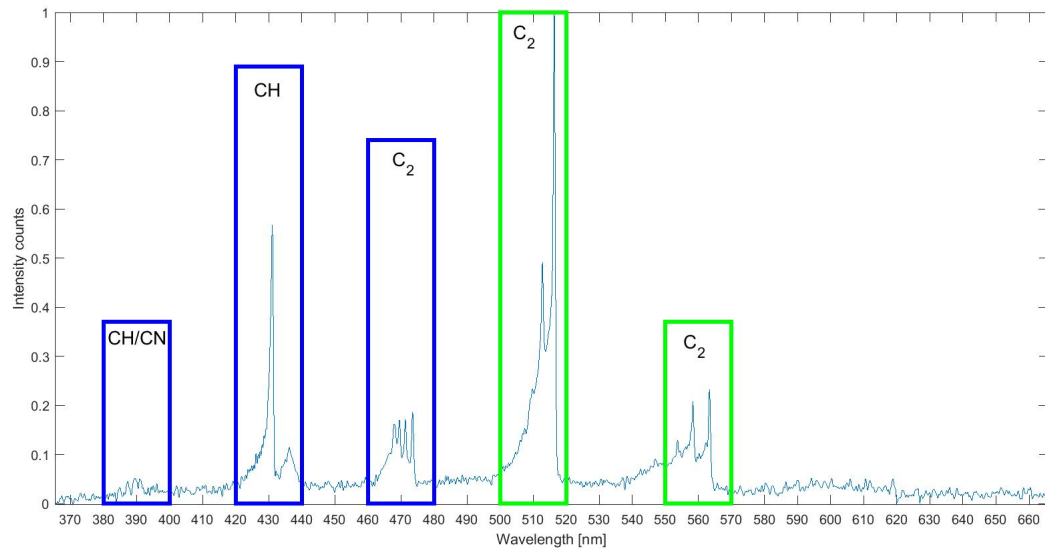


Figure 6.13: The intensity of each band group plotted on top of the spectrum collected by the point-spectrometer.

### 6.3.3. IMAGE SKEWING AND SPATIAL DISTRIBUTION ANALYSIS

In this subsection, the results from vertical separation configuration will be used to analyze the possible skewing caused by the imaging system. The main focus will be on the two peaks with the highest intensity and the most distinctive feature: $C_2$ ($514nm$) and CH ($431nm$). After an understanding of image skewing, the spatial distribution of these 2 peaks in a conical Bunsen flame will also be discussed.

#### THE INFLUENCE OF INCIDENCE ANGLES ON IMAGE SKEWING

In order to study the relation between image skewing and incidence angle on the grating surface, a series of grating deflection angles are chosen from $0°$ to $45°$ in a step of $15°$. The result is shown in the picture below. The incidence angle from left to right is $0°$, $15°$, $30°$, $45°$ respectively. As can be found in the picture that as the incidence angle increases across the Littrow angle $15°$, the stretching of CH ($431nm$) image along the direction of dispersion is decreasing obviously. The anamorphic magnification factors for the image of CH ($431nm$) are measured to be 1.31, 1.01, 0.87, 0.74, which are very close to the theoretical values: 1.17, 1, 0.87, 0.72 calculated by anamorphic magnification formula.



Figure 6.14: The influence of incidence angles on image skewing. From left to right, the incidence angles are $0°$, $15°$, $30°$, $45°$ respectively

IMAGE SKEWING ANALYSIS IN LITTROW CONFIGURATION

Since the spatial distribution of these radicals in a conical Bunsen flame is unknown and the real shape of each spectral image may vary slightly, the information about the amount of skewing in the spectral images cannot be re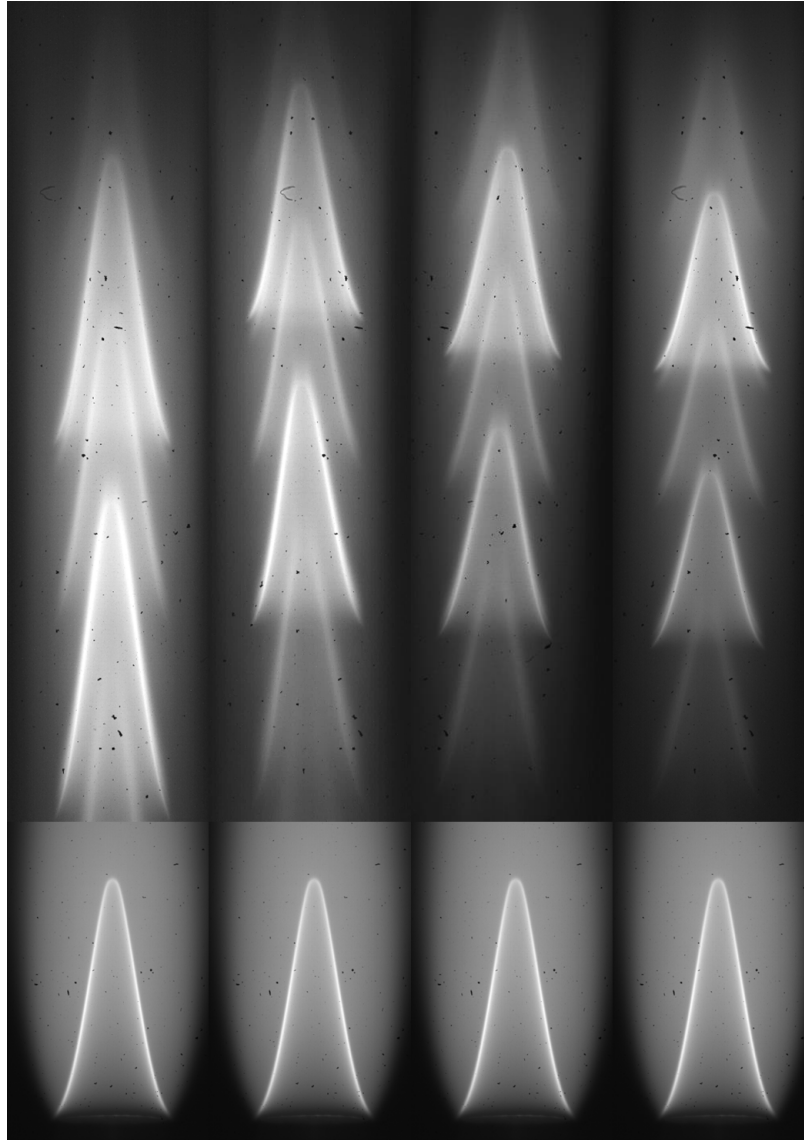trieved directly from the pictures. Therefore a calibration target with a fixed shape and known dimension needs to be implemented.

Initially, the checkerboard target tested in the previous monochromatic synthetic flame design is investigated, however giving a very unsatisfactory result. Strong overlapping of spectral images between adjacent wavelengths, as shown below, makes it impossible to discern the image skewing details.
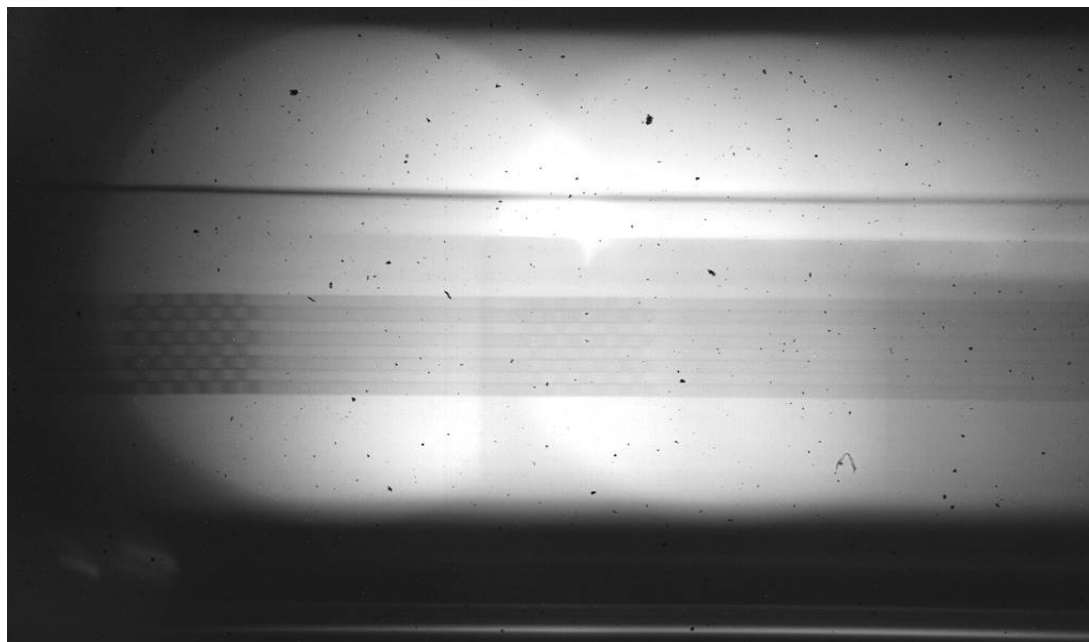


Figure 6.15: 1st order dispersion of the checkerboard target illuminated by the Bunsen flame, captured by the vertical dispersion configuration

So in this experiment, eventually the right triangle target is used, which gives a very good spatial dispersion, as shown below.
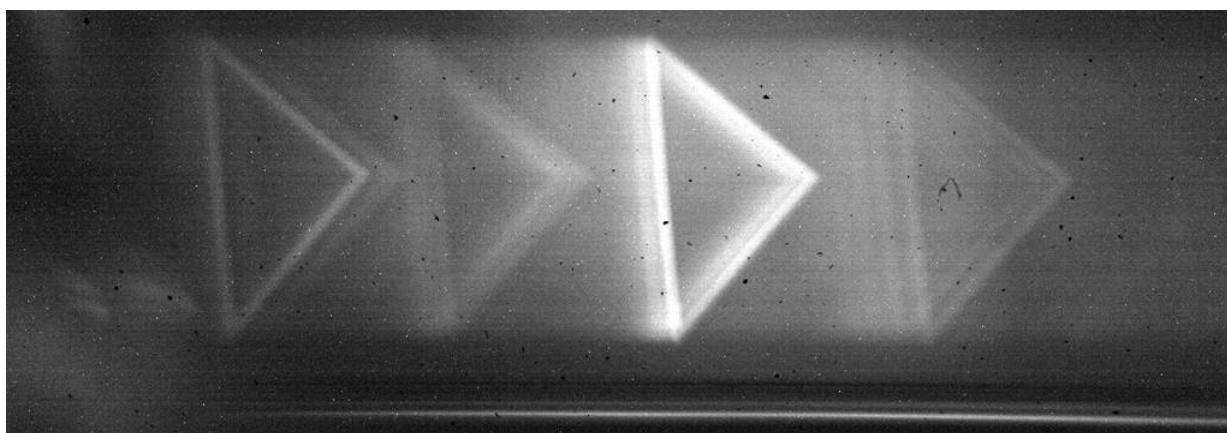


Figure 6.16: 1st order dispersion of the triangle target illuminated by the Bunsen flame, captured by the vertical dispersion configuration.

The transparency triangle target is illuminated by the Bunsen flame, so the wavelength of each triangle can be correlated to the spectrum data captured by the point spectrometer. In this way, the skewing of the image can be verified in these spectral triangles by measuring their geometries. The author has measured the height and the vertex angle, which shows that there is almost no difference between the 2 geometries. The height, as shown in the figure below, is 136.44 pixels for CH ($431nm$) triangle while that of the $C_2$ ($514nm$) is

139.50 pixels. Definitely the $C_2$ ($514nm$) triangle has been stretched more but the difference is only 3.14 pixels ($33\ \mu m$), which are 1.64 pixels less than the theoretical value calculated using anamorphic magnification formula. This small deviation could be attributed to the compensation of perspective distortion, which works in the opposite direction, compressing the image shape.

The vertex angle difference is also almost negligible, which is 89.5° for CH ($431nm$) triangle and 88.3° for $C_2$ ($514nm$) triangle. Such a small difference is thus highly influenced by the measurement errors. The author has measured several times and the value provided here is actually an average of all the measurements. Depending on how these geometries are measured, the difference can even be much smaller.
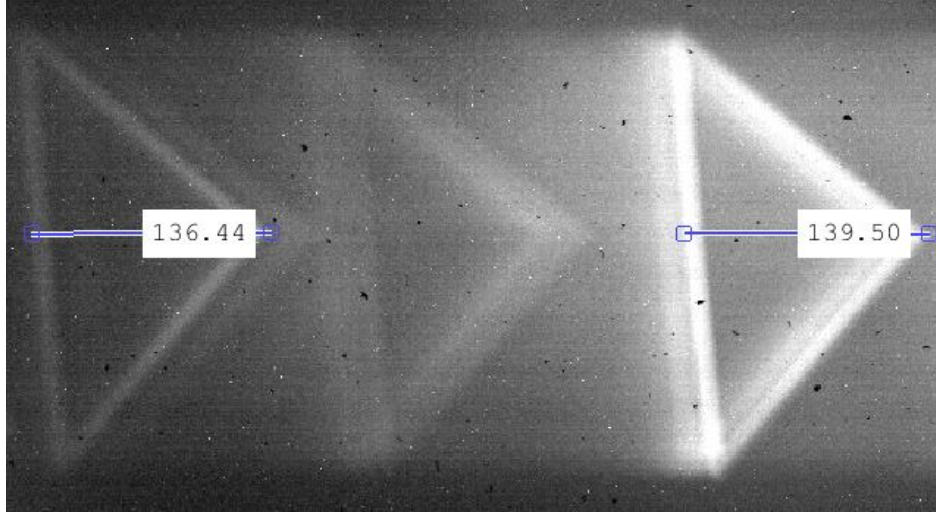


Figure 6.17: A zoomed-in view of the 1st order dispersion of the triangle target illuminated by the Bunsen flame.

In conclusion, this setup under the condition of Littrow configuration, 15° incidence angle, has almost negligible image skewing.

### Spatial distribution of $C_2$ ($514nm$) and CH ($431nm$)

The spectral images of CH ($431nm$) and $C_2$ ($514nm$) have been zoomed in and measured as shown in the figure below. Since it has been proved previously that there is a negligible image skewing in this configuration, the geometries of the 2 spectral images could be treated approximately skewing free. However it is interesting to see that no matter how these two conical shapes are measured, the spectral image of CH ($431nm$) always has a narrower bottom and a longer height, which is different from what has been found in the right triangle case. If the two spectral images have exactly the same size, even considering image skewing effect, the image of $C_2$ ($514nm$) should be somehow elongated instead of being shortened. Therefore, their spatial distribution must be non-identical. In comparison to CH ($431nm$), the spectral image of $C_2$ ($514nm$) should have a shorter height while longer bottom, as demonstrated in the schematic diagram below.



(a) The spectral image of CH ($431nm$)     (b) The spectral image of $C_2$ ($514nm$)

Figure 6.18: Geometry measurement on the spectral image of CH ($431nm$) and $C_2$ ($514nm$).



Figure 6.19: A schematic diagram of possible spatial distribution: CH ($431nm$) and $C_2$ ($514nm$) at the equivalence ratio of 1.2.

# 7

# CONCLUSIONS AND RECOMMENDATIONS

This chapter will review and conclude the master thesis research, identify the main contributions and limitations, and in the end discuss the possible directions for future research.
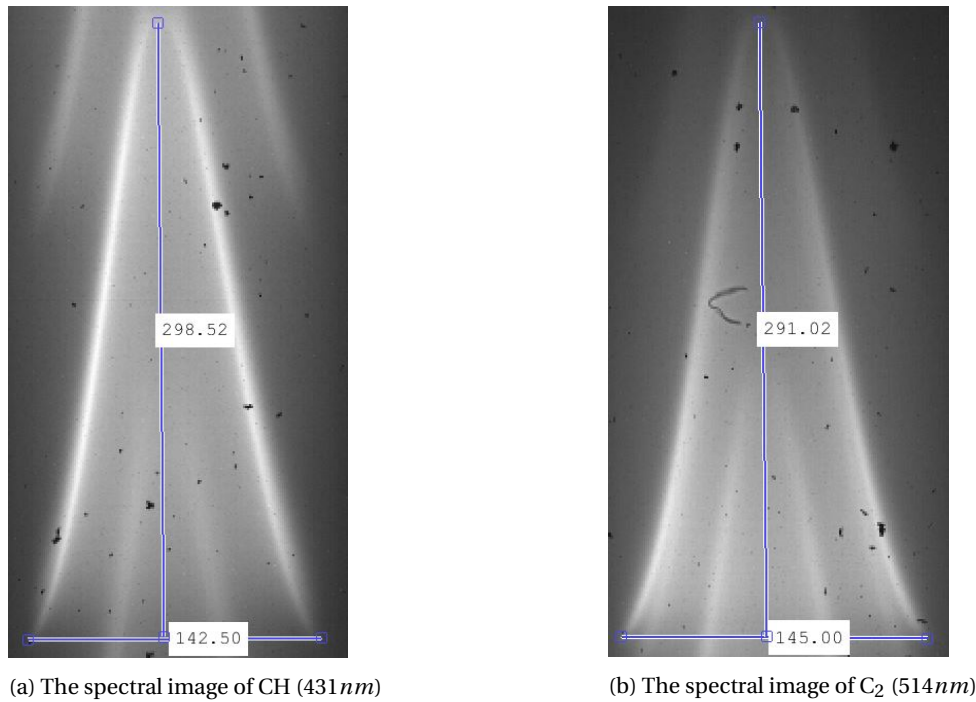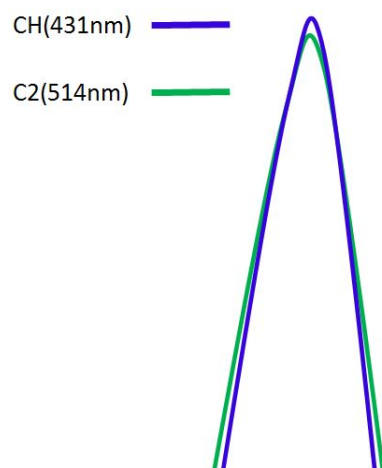
## 7.1. CONCLUSIONS

In summary, 2 setups were proposed and discussed in this thesis project. The first setup called the design of a monochromatic synthetic flame mainly investigated on the diffraction grating anamorphic magnification and its automatic calibration using a checkerboard target. The second setup called the design of a slitless spectrometer studied the spatial distribution of CH and $C_2$ radicals in the spectral range between 350 $nm$ and 700 $nm$. The feasibility of achieving distortion-free spectral images in Littrow configuration was also discussed in the second setup.

Basically 3 main conclusions can be drawn from the results reported in this thesis.

1. The diffraction grating anamorphic magnification for an imaging spectrometer can be totally controlled by choosing different incidence angles and the experimental results are highly agreed with the theoretical calculation. This type of image skewing will totally disappear if the grating is set to a certain angle called Littrow angle.

2. The idea of slitless spectrometer used in flame emission spectroscopy is feasible. It is able to not only produce clear spectral images of flame radicals but also have negligible image distortion within a certain field of view and a certain span of wavelength range.

3. Depending on the equivalence ratio, the spatial distribution of CH ($431nm$) and $C_2$ ($514nm$) are slightly different in a conical Bunsen flame. The profile of $C_2$ ($514nm$) is shorter in height and wider at the bottom when the equivalence is set to be 1.2.

The main contribution of this research is that the concept of a conventional slit spectrometer has been expanded to a slitess spectrometer. By expanding this concept, a more appropriate definition of collimation is given and the resulting distortion due to an open of the slit is also investigated thoroughly. The concept of anamorphic magnification which is commonly ignored in a conventional slit spectrometer experiment is studied and this effect is now under great control. More remarkably, in contrast to conventional scanning spectrometer, this slitless spectrometer is capable of obtaining whole-field-of-view chemiluminescence information at a specific combustion time point, which makes it powerful to study more complex time-changing flame structures such as a turbulence flame. In a very short exposure time, the whole natural chemiluminescence zone can be frozen, and the spatial distribution of its component radicals can be obtained simultaneously.

The main limitation of this research is that the resolution of the acquired spectral images is still limited to some degree so that the measurement of their dimension, which comes down to several micrometers, is more prone to be influenced by personal measurement errors. The lenses used are also not corrected for chromatic and spherical aberrations, which could contribute to the reduction in resolution. Another limitation is that the spectral response of this slitless spectrometer is not calibrated, meaning that users cannot rely on the

intensity of each spectral images and the information about relative content of each flame radical cannot be retrieved from this experiment by comparing their amplitude of intensity. Moreover, another interesting spectrum of OH which locates at $308nm$ cannot be recorded because of the extremely low spectral response for not only the optics but also the camera sensor in the UV region. In addition to the missing spectrum calibration, a proper calibration of image distortion, although nearly negligible, is also lacking. The widely-used checkerboard target for machine vision fails to calibrate this slitless spectrometer due to strong overlapping of adjacent spectral images.

## 7.2. RECOMMENDATIONS

### 7.2.1. IMAGE RESOLUTION IMPROVEMENT

As mentioned above, the limitation in resolution results in a problem of precisely defining the boundary of each spectral profile. So in order to obtain more accurate spatial distribution of these radicals, one could think of how to increase the resolution of these spectral images. A simple way to increase the optical resolution is implementing optics corrected for chromatic and spherical aberrations. Moreover, it is also worth researching on the influence of the relative size of an object. If a decrease in the relative size of an object in comparison to the collimating lens gives rise to the system resolution, one could probability think of using an imaging system to form a demagnified image of the original object first or simply employing a larger collimating lens. Additionally, the future investigation could be not only on increasing optical resolution of the imaging system design but also on manipulating the flame structure itself for achieving a more distinguishable chemiluminescence zone.

### 7.2.2. SPECTRAL AND SPATIAL CALIBRATION

As mentioned in the limitation, the spectral response for all the lenses, diffraction grating and the camera sensor is wavelength-dependent. So for obtaining the real intensity of each radical, a spectral calibration method is necessary to be developed for the future research.

The automatic calibration of an object of single wavelength is successful in this thesis. However, when it comes to a real flame , the current checkerboard target, as a matter of the pattern's shape, fails to calibrate the spectral images because of the large overlapping region, as shown before. The second calibration target, right triangle target, although has not been actually used to calibrate the image, is however turned out to be efficient in reducing the overlapping region. So for a future research, one could possibly continue to develop this triangle shape and figure out a supporting calibration method based on that shape.

### 7.2.3. CHROMATIC SYNTHETIC FLAME DESIGN

For evaluating the performance of a flame emission spectroscopy imaging system, a more controllable light source used to simulate a real flame is worthy to study. In this thesis, a monochromatic synthetic flame, an object illuminated by a red HeNe laser, has been studied, which is however limited to a single wavelength and the illumination type of the flame is also not properly simulated. So for a research in the future, one could think of how to generate a light source that has a well-defined shape, the same illumination type as a real flame and a narrow-band spectrum of variable wavelengths.

# BIBLIOGRAPHY

[1] H. Hottel and W. Hawthorne, *Diffusion in laminar flame jets,* in *Symposium on Combustion and Flame, and Explosion Phenomena*, Vol. 3 (Elsevier, 1948) pp. 254–266.

[2] T. O. University, *How lenses and mirrors work.* (2011), [Online; accessed 19-April-2018].

[3] *Astronomical optics,* (2014), [Online; accessed 19-April-2018].

[4] Wikipedia contributors, *Chromatic aberration — Wikipedia, the free encyclopedia,* (2018), [Online; accessed 19-April-2018].

[5] S. Mirasol-Menacho, A. Planells-Pérez, A. Barba-Sevillano, J. Segura-Garcia, M. Cobos-Serrano, and A. Giménez-Pérez, *Development of a hmd for virtual acoustics. application in a world heritage (unesco) building from the valencian civil gothic,* in *International Conference on Augmented Reality, Virtual Reality and Computer Graphics* (Springer, 2016) pp. 241–250.

[6] Wikipedia contributors, *Distortion (optics) — Wikipedia, the free encyclopedia,* (2018), [Online; accessed 7-May-2018].

[7] W. Schrenk, *Analytical atomic spectroscopy* (Springer Science & Business Media, 2012).

[8] Wikipedia contributors, *Prism — Wikipedia, the free encyclopedia,* (2018), [Online; accessed 14-May-2018].

[9] H. contributor, *The rayleigh criterion,* [Online; accessed 14-May-2018].

[10] Thorlabs contributors, *Introduction to diffraction grating,* (2018), [Online; accessed 7-May-2018].

[11] ScienceSourceimages contributors, *Light dispersed by diffraction grating,* [Online; accessed 7-May-2018].

[12] C. A. Palmer and E. G. Loewen, *Diffraction grating handbook* (Newport Corporation New York, 2005).

[13] N. A. Hagen, L. S. Gao, T. S. Tkaczyk, and R. T. Kester, *Snapshot advantage: a review of the light collection improvement for parallel high-dimensional measurement systems,* Optical Engineering **51**, 111702 (2012).

[14] TUDelft, *Measurement of the laminar burning velocity of methane,* (2018), in the course combustion for propulsion and power technologies.

[15] Thorlabs contributors, *Compact ccd spectrometers,* (2018), [Online; accessed 14-May-2018].

[16] K-MAC contributors, *Spectrometer,* [Online; accessed 14-May-2018].

[17] Thorlabs contributors, *N-bk7 plano-convex lenses (ar coating: 350 - 700 nm),* (2018), [Online; accessed 14-May-2018].

[18] Thorlabs contributors, *Visible transmission gratings,* (2018), [Online; accessed 14-May-2018].

[19] Dataray contributors, *Wincamd-lcm – usb 3.0, 1 cmos beam profiler system,* [Online; accessed 14-May-2018].

[20] J. Krabicka and G. Lu, *Visualisation and characterisation of flame radical emissions through intensified spectroscopic imaging,* in *Journal of Physics: Conference Series*, Vol. 178 (IOP Publishing, 2009) p. 012041.

[21] A. Gaydon, *The spectroscopy of flames* (Springer Science & Business Media, 2012).

[22] Y. MIZUTANI, K. NAKABE, Y. MATSUMOTO, T. SAEKI, and T. MATSUI, *Processing of luminescent radical images for flame diagnostics,* JSME international journal. Ser. 2, Fluids engineering, heat transfer, power, combustion, thermophysical properties **32**, 455 (1989).

[23] R. Bombach and B. Käppeli, *Simultaneous visualisation of transient species in flames by planar-laser-induced fluorescence using a single laser system,* Applied Physics B: Lasers and Optics **68**, 251 (1999).

[24] B. H. Timmerman and P. Bryanston-Cross, *Optical investigation of heat release and nox production in combustion,* in *Journal of Physics: Conference Series,* Vol. 85 (IOP Publishing, 2007) p. 012007.

[25] S. Karnani and D. Dunn-Rankin, *Visualizing ch\* chemiluminescence in sooting flames,* Combustion and Flame **160**, 2275 (2013).

[26] G. Zizak, *Flame emission spectroscopy: fundamentals and applications,* (2000).

[27] D. Alviso, M. Mendieta, J. Molina, and J. C. Rolón, *Flame imaging reconstruction method using high resolution spectral data of oh\*, ch\* and c2\* radicals,* International Journal of Thermal Sciences **121**, 228 (2017).

[28] L. G. Barreta, C. J. da Rocha, D. Carinhana Jr, M. Esther, A. C. d. O. Sbampato, and A. M. dos Santos, *Emission spectroscopy of ch radical to determine the temperature of ethanol flame,* CEP **12228**, 840 (2003).

[29] B. Higgins, M. McQuay, F. Lacas, and S. Candel, *An experimental study on the effect of pressure and strain rate on ch chemiluminescence of premixed fuel-lean methane/air flames,* Fuel **80**, 1583 (2001).

[30] T. Muruganandam, B. Kim, R. Olsen, M. Patel, B. Romig, J. Seitzman, and B. Zinn, *Chemiluminescence based sensors for turbine engines,* in *39th AIAA/ASME/SAE/ASEE Joint Propulsion Conference and Exhibit* (2003) p. 4490.

[31] J. F. James, R. S. Sternberg, and S. A. Rice, *The design of optical spectrometers,* Physics Today **23**, 55 (1970).

[32] G. R. Harrision, R. C. Lord, and J. R. Loofbourow, *Practical spectroscopy* (Prentice-Hall. Inc.; New York, 1948).

[33] S. Pfadler, F. Beyrau, and A. Leipertz, *Flame front detection and characterization using conditioned particle image velocimetry (cpiv),* Optics Express **15**, 15444 (2007).

[34] N. Dam, *An introduction to Laser Diagnostics for Combustion Spectroscopy for Mechanical Engineers* (2016).

[35] M. Bigas, E. Cabruja, J. Forest, and J. Salvi, *Review of cmos image sensors,* Microelectronics journal **37**, 433 (2006).

[36] M. W. Davidson, *Numerical aperture.* (2018), [Online; accessed 19-April-2018].

[37] R. Mavrodineanu, R. Mavrodineadu, and C. T. J. Alkemade, *Analytical Flame Spectroscopy: Selected Topics* (Springer-Verlag, 1970).

[38] D. J. Schroeder, *10. diffraction grating instruments,* in *Astrophysics,* Methods in Experimental Physics, Vol. 12, edited by N. Carleton (Academic Press, 1974) pp. 463 – 489.

[39] B.E.Sauer, *The grating spectrometer,* (2007), [Online; accessed 7-May-2018].

[40] J. Allington-Smith, *Dispersive astronomical spectroscopy,* Image **500**, 2 (2002).

[41] Horiba contributors, *Monochromators spectrographs,* (2018), [Online; accessed 7-May-2018].

[42] N. A. Hagen and M. W. Kudenov, *Review of snapshot spectral imaging technologies,* Optical Engineering **52**, 090901 (2013).

[43] DxOMark contributors, *Nikon af nikkor 50mm f/1.8d mounted on nikon d800e : Tests and reviews,* [Online; accessed 14-May-2018].

[44] Matlab contributors, *Single camera calibration,* [Online; accessed 14-May-2018].